

# Bulletin of Volcanology

## The Ventotene Volcanic Ridge: a newly explored complex in the central Tyrrhenian Sea (Italy) --Manuscript Draft--

<b>Manuscript Number:</b>	BUVO-D-16-00095R2
<b>Full Title:</b>	The Ventotene Volcanic Ridge: a newly explored complex in the central Tyrrhenian Sea (Italy)
<b>Article Type:</b>	Research Article
<b>Corresponding Author:</b>	Marco Cuffaro, Ph.D. Consiglio Nazionale delle Ricerche Roma, ITALY
<b>Corresponding Author Secondary Information:</b>	
<b>Order of Authors:</b>	Marco Cuffaro, Ph.D. Eleonora Martorelli Alessandro Bosman Alessia Conti Sabina Bigi Filippo Muccini Luca Cocchi Marcol Ligi Giovanni Bortoluzzi Davide Scrocca Simonepietro Canese Francesco Chiocci Aida Maria Conte Carlo Doglioni Cristina Perinelli
<b>Funding Information:</b>	
<b>Abstract:</b>	<p>New high-resolution geophysical data collected along the eastern margin of the Tyrrhenian backarc basin, in the Pontine Islands area, reveal a ~NW-SE elongated morphological high, the Ventotene Volcanic Ridge (VR), located on the northern edge of the Ventotene Basin. High-resolution multibeam bathymetry, combined with magnetic data, multi- and single-channel seismic profiles, and ROV dives suggest that VR results from aggregation of a series of volcanic edifices. The summit of these volcanoes is flat and occurs at about 170 m water depth. Given their depths, we propose that flat morphologies were probably caused by surf erosion during Quaternary glacial sea level lowstands. Seismic stratigraphy together with magnetic data suggest that the volcanic activity in this area is older than 190-130 ka age and may be coeval with that of Ventotene Island (Middle Pleistocene). The submarine volcanoes, located 25 km north of Ventotene, are part of a ~E-W regional volcanic alignment and extend the Pontine volcanism landward toward the Gaeta bay. Integration of structural data from multichannel seismic profiles in this sector of the eastern Tyrrhenian margin indicates that several normal and/or transtensional faults, striking WNW-ESE, NNW-SSE and NE-SW, offset the basement and form alternating structural highs and depressions filled by thick, mostly undeformed, sedimentary units. Arc-related magmatism is widespread in the study area, where the VR is placed at the hangingwall of the west-directed Apennines subduction zone, which is undergoing</p>

	<p>tensional and transtensional tectonics. Bathymetric and topographic evidence shows that VR lies in between a major NE-SW trending escarpment east of Ponza and a NE-SW trending graben southwest of the Roccamonfina volcano; a NE-SW transfer zone that accommodate the extension along this segmented portion of the margin. This suggests that the interaction between NE-SW and NW-SE trending fault systems acts a structural control on location of eruptive centres, given that main volcanic edifices develop along the NW-SE direction, compatible with the extensional setting of the Tyrrhenian basin.</p>
<b>Response to Reviewers:</b>	<p>Please, find the detailed answers to the points you highlighted in the attached file “cuffaro_et_al_16_detailed_answers_R1.doc”, and the changes improved or added in the manuscript, highlighted in red, in the attached file “cuffaro_et_al_2016_bull_volcanol_REV_R1_submission.docx”.</p>

[Click here to view linked References](#)

# The Ventotene Volcanic Ridge: a newly explored complex in the central Tyrrhenian Sea (Italy)

Marco Cuffaro<sup>1\*</sup>, Eleonora Martorelli<sup>1</sup>, Alessandro Bosman<sup>1</sup>,  
Alessia Conti<sup>2</sup>, Sabina Bigi<sup>2</sup>, Filippo Muccini<sup>3</sup>, Luca Cocchi<sup>3</sup>, Marco Ligi<sup>4</sup>, Giovanni  
Bortoluzzi<sup>4</sup>, Davide Scrocca<sup>1</sup>, Simonepietro Canese<sup>5</sup>, Francesco L. Chiocci<sup>2</sup>, Aida M. Conte<sup>6</sup>,  
Carlo Doglioni<sup>2,3</sup>, Cristina Perinelli<sup>2</sup>

<sup>1</sup>*Istituto di Geologia Ambientale e Geoingegneria, CNR, c/o Dipartimento di Scienze della Terra, Università Sapienza, P.le A. Moro 5, 00185 Roma, Italy.*

<sup>2</sup>*Dipartimento di Scienze della Terra, Università Sapienza, P.le A. Moro 5, 00185 Roma, Italy.*

<sup>3</sup>*Istituto Nazionale di Geofisica e Vulcanologia, Roma2, Via Pezzino Basso 2, 19025, Fezzano (La Spezia), Italy.*

<sup>4</sup>*Istituto di Scienze Marine, CNR, Via Gobetti 101, 40129, Bologna, Italy.*

<sup>5</sup>*Istituto Superiore per la Ricerca e la Protezione Ambientale (ISPRA), CRA15 III Dipartimento Tutela degli Habitat e della Biodiversità Marina, Via Vitaliano Brancati 60, Roma, Italy.*

<sup>6</sup>*Istituto di Geoscienze e Georisorse, CNR, c/o Dipartimento di Scienze della Terra, Università Sapienza, P.le Aldo Moro 5, I-00185, Roma, Italy.*

\*Corresponding Author:

Istituto di Geologia Ambientale e Geoingegneria (IGAG), CNR  
c/o Dipartimento di Scienze della Terra  
Sapienza Università di Roma  
P.le A. Moro 5,  
I-00185 Rome, ITALY  
Phone: +39 06 4991 4575  
Fax: +39 06 4454729  
e-mail: marco.cuffaro@igag.cnr.it

## 43 **Abstract**

44 New high-resolution geophysical data collected along the eastern margin of the Tyrrhenian  
45 backarc basin, in the Pontine Islands area, reveal a ~NW-SE elongated morphological high, the  
46 Ventotene Volcanic Ridge (VR), located on the northern edge of the Ventotene Basin. High-  
47 resolution multibeam bathymetry, combined with magnetic data, multi- and single-channel  
48 seismic profiles, and ROV dives suggest that VR results from aggregation of a series of volcanic  
49 edifices. The summit of these volcanoes is flat and occurs at about 170 m water depth. Given  
50 their depths, we propose that flat morphologies were probably caused by surf erosion during  
51 Quaternary glacial sea level lowstands. Seismic stratigraphy together with magnetic data suggest  
52 that the volcanic activity in this area is older than 190-130 ka age and may be coeval with that of  
53 Ventotene Island (Middle Pleistocene). The submarine volcanoes, located 25 km north of  
54 Ventotene, are part of a ~E-W regional volcanic alignment and extend the Pontine volcanism  
55 landward toward the Gaeta bay. Integration of structural data from multichannel seismic profiles  
56 in this sector of the eastern Tyrrhenian margin indicates that several normal and/or transtensional  
57 faults, striking WNW-ESE, NNW-SSE and NE-SW, offset the basement and form alternating  
58 structural highs and depressions filled by thick, mostly undeformed, sedimentary units. Arc-  
59 related magmatism is widespread in the study area, where the VR is placed at the hangingwall of  
60 the west-directed Apennines subduction zone, which is undergoing tensional and transtensional  
61 tectonics. Bathymetric and topographic evidence shows that VR lies in between a major NE-SW  
62 trending escarpment east of Ponza and a NE-SW trending graben southwest of the Roccamonfina  
63 volcano; a NE-SW transfer zone that accommodate the extension along this segmented portion  
64 of the margin. This suggests that the interaction between NE-SW and NW-SE trending fault  
65 systems acts a structural control on location of eruptive centres, given that main volcanic edifices  
66 develop along the NW-SE direction, compatible with the extensional setting of the Tyrrhenian  
67 basin.

68 **Keywords:** Submarine volcanic edifices, Pontine Islands, High-resolution geophysical data

69

## 70 **1 Introduction**

71 Submarine volcanoes are difficult to study because of the lack of direct access; although volcanic  
72 cones are expected to be common in volcanically active provinces, there are few seismic datasets  
73 revealing their internal structures, surprisingly showing peculiar differences. During the last  
74 decades, marine geology research has allowed a better understanding of their nature by  
75 collecting a large amount of geophysical data, such as magnetic, seismic, and bathymetric,  
76 integrated with ROV visual inspections, coring and sampling (Arnulf et al, 2014; Conte et al,  
77 2014; Iezzi et al, 2014; Bani et al, 2015; Honsho et al, 2015; Loreto et al, 2015; Rotella et al,  
78 2015, among the others).

79 Geophysical data, such as multibeam bathymetry, multi- and single-channel seismic and  
80 magnetic investigations are among the most suitable methods to explore volcanic areas and their  
81 integration may significantly improve detection and characterization of buried and outcropping  
82 bodies. Recently, advances in seafloor mapping have greatly contributed to our knowledge of the  
83 morphological aspects of submarine volcanic edifices and insular volcanoes flanks (e.g., Bosman  
84 et al, 2009), especially those of the Pontine Islands in the central-eastern Tyrrhenian Sea basin  
85 (e.g., Casalbore et al, 2014a; Ingrassia et al, 2015, and references therein).

86 Submarine exploration also provided useful information on how submarine volcanoes work.  
87 Their underwater activity is different from that of the subaerial volcanoes, showing large  
88 hydrothermal systems (Gruen et al, 2014; Italiano et al, 2014), or presenting petrological and  
89 geochemical alterations of the erupted products, quickly cooled by seawater. Sometimes the

90 water-magma interaction creates explosions, whose products are partially deposited on the  
91 bottom and dispersed by sea currents; in addition, the occurrence of these deposits along  
92 submarine slopes can be the cause of slope instability and submarine landslides (Caratori Tontini  
93 et al, 2010; Romagnoli et al, 2013a; Bosman et al, 2014; Day et al, 2015; Honsho et al, 2015;  
94 Sibrant et al, 2015). In Italy, submarine volcanic activity is concentrated in the Tyrrhenian Sea  
95 and the Sicily channel, two areas characterized by different geodynamic settings (Caló and  
96 Parisi, 2014; Carminati et al, 2010; Palano et al, 2012). With more than 20 submarine active  
97 volcanoes, including the Marsili, the Europe's largest underwater volcano, the central and  
98 southern sectors of the Tyrrhenian Sea are among the most volcanically active areas of the  
99 Mediterranean Sea. Some underwater volcanoes are active and sometimes manifest their  
100 presence by releasing gases and **deforming** very slowly (Dekov and Savelli, 2004; Bortoluzzi et  
101 al, 2010); others, extinct, form underwater ridge or seamounts. Marsili, Vavilov and Magnaghi  
102 are the main submarine volcanoes, together with volcanic complexes of Palinuro, Glauco, Eolo,  
103 Sisifo, and Enarete, as well as the volcanic areas in the Sicily Channel (Calanchi et al, 1989;  
104 Catalano et al, 2014; Conte et al, 2014, and references therein).

105 In this geological **context**, the Pontine Islands (central Tyrrhenian Sea, Italy) consist of a 50-km-  
106 long chain of five volcanic islands (Ponza I., Zannone I. and Palmarola I. to the west; Ventotene  
107 I. and Santo Stefano I. to the east) and islets, located between the Circeo Promontory and the  
108 Gaeta Bay (Fig. 1). The Pontine Islands have developed during the Plio-Pleistocene extensional  
109 phase, related to the opening of the Vavilov basin (Zitellini et al, 1984). The intense volcanic  
110 activity in the area may be linked to the west-dipping subduction of the Adria plate under the  
111 Eurasia plate, and to the back-arc extension, which opened the Tyrrhenian Sea in an east-west  
112 direction and caused the extensional tectonics along the eastern Tyrrhenian margin (Cadoux et  
113 al, 2005; Carminati et al, 2010, and references therein), resulting in magmatic events along the  
114 Latium-Campanian shelf, onshore (e.g. Roccamonfina, Campi Flegrei and Vesuvio) and offshore

115 (e.g., Ischia-Procida) (Fig. 1). In addition, buried volcanic edifices were drilled onshore at Parete  
116 and Villa Literno (Torrente and Milia, 2013, and references therein), and submarine and buried  
117 complexes were detected at sea, south of the Ponza Island (e.g., the Botte Rock, Chiocci and  
118 Martorelli, 2015; Ingrassia et al, 2015), using multibeam bathymetry, and in the Gaeta Bay  
119 (Bartole, 1984; de Alteriis et al, 2006; Torrente and Milia, 2013), from seismic reflection profiles  
120 and magnetic data (Fig. 1). The southeastward shift of the volcanic activity (Scrocca et al, 2003;  
121 Peccerillo, 2005) may be caused by the slab retreat and steepening, or by a process of slab break-  
122 off starting in the Pliocene (Doglioni et al, 1999; Argnani and Savelli, 1999; Cadoux et al, 2005;  
123 Bortoluzzi et al, 2010).

124 Although many data have been collected in the last decades, in this sector of the Tyrrhenian Sea,  
125 some areas are not still completely explored. Newly acquired high-resolution geophysical data  
126 (swath bathymetry, magnetometry, chirp, multichannel seismic reflection) and ROV dives led to  
127 the first exploration and mapping of a NW-SE-oriented, elongated and partially buried  
128 morphological high, here named the Ventotene Volcanic Ridge (VR), offshore Gaeta, north of  
129 Ventotene Island. The integration of data collected during several cruises in the area, including  
130 some specifically collected for this purpose, provides a good-quality morpho-structural picture of  
131 the region, suggesting a volcanic nature for the VR, closely linked to the local and regional fault  
132 patterns. We present and discuss hereinafter the volcanological and tectonic setting of the VR, in  
133 the light of the extensional deformation styles related to the opening of the Tyrrhenian Sea.

134

## 135 **2 Geological setting**

136 The Pontine Islands are located on the central-eastern continental margin of the Tyrrhenian Sea  
137 basin (Fig.1). The opening of the Tyrrhenian Sea back arc occurred in the hangingwall of the

138 Neogene to Present, eastward retreating, subduction zone associated with the development of the  
139 Apennines-Maghrebides chain (among many others, Malinverno and Ryan, 1986; Doglioni,  
140 1991; Patacca et al, 1992; Faccenna et al, 1997; Rosenbaum and Lister, 2004). Since middle-late  
141 Miocene the development of the Tyrrhenian back arc basin has been accompanied by crustal  
142 thinning, faulting and volcanic activity. The extension and the related magmatism migrated from  
143 west to east (e.g., Zitellini et al, 1986; Kastens et al., 1988; Beccaluva et al., 1990; Patacca et al,  
144 1992; Mauffret et al, 1999; Serri et al, 2001; Doglioni et al, 2004; Scrocca et al, 2012; Moeller et  
145 al, 2013; Buttinelli et al, 2014).

146 In our study area (Fig. 1), the extensional tectonics were responsible for the formation of the  
147 very steep continental escarpment, for the formation of intraslope basins (e.g., the Ventotene and  
148 Palmarola basins), and for the general “horst and graben” setting of the continental margin. The  
149 main structural directions affecting the Pontine sector are NW-SE, NE-SW and E-W (De Rita et  
150 al, 1986). The Pliocene to late Pleistocene intense volcanic activity (Cadoux et al, 2005, and  
151 references therein), which gave rise to the Pontine Islands, has been speculated to be related to  
152 this tectonic phase (Cadoux et al, 2005).

153 Between the Circeo Promontory and the Gaeta Bay, the shelf has a width of 25 km, and is  
154 connected to the Vavilov bathyal plain through a very steep escarpment NW-SE oriented.  
155 Maximum shelf extension is reached offshore Circeo Promontory (more than 40 km), where a  
156 NE-SW elongate structural high divides the two major areas of sedimentation: the intraslope  
157 basins of Palmarola (to the NW) and Ventotene (to the SE), both filled by Plio-Pleistocene  
158 siliciclastic sequences (Zitellini et al, 1984).

159 The western sector of the Archipelago includes Ponza, Zannone and Palmarola islands (Fig. 1),  
160 which developed during two main volcanic cycles dated between 4.2–2.9 Ma and 1.6–0.9 Ma  
161 (Cadoux et al, 2005). Zannone and most part of Ponza island were built during the Pliocene

162 cycle, with the emplacement of high-K calc-alkaline rhyolites. The Pleistocene cycle started at  
163 about 1.6 Ma with the eruption of peralkaline trachytes and rhyolites belonging to transitional  
164 rock-series (Conte et al, 2016) that formed the entire Island of Palmarola. A small outcrop dated  
165 at 1.2 Ma (Conte and Dolfi, 2002, and references therein) occurs in the southeastern part of  
166 Ponza island. The Pleistocene magmatic phase ended with the emplacement of shoshonitic  
167 trachytes (1.0 Ma) erupted in the southeastern part of Ponza island (Mt. Guardia lava dome, Le  
168 Formiche shoals). These products represent the first episode of the K-alkaline magmatism that  
169 successively developed southeastward at "La Botte" neck, in the eastern Pontine Islands  
170 (Ventotene and S. Stefano) and more in general in the Magmatic Campanian Region. Ventotene  
171 and S. Stefano represent the tip of a large strato-volcano emplaced at the center of the subsiding  
172 Ventotene basin and bounded southward by NW-SE regional tectonic structures (Marani and  
173 Gamberi, 2004). Ventotene and S. Stefano islands are composed of basaltic to trachytic lavas  
174 (0.80-0.48 Ma; Metrich et al, 1988) unconformably covered by pyroclastic products erupted in  
175 the time span 0.2 Ma (Metrich et al, 1988) to 41 ka (Alessio et al, 1974).

176

### 177 **3 Methods**

178 Geophysical data were collected from 2010 to 2014, with the R/V Urania of the Consiglio  
179 Nazionale delle Ricerche (CNR), and R/V Astrea of the Istituto Superiore per la Protezione e la  
180 Ricerca Ambientale (ISPRA). Oceanographic cruises TIR-10 ([http://www.ismar.cnr.it/products/  
181 reports-campagne/2010-2019](http://www.ismar.cnr.it/products/reports-campagne/2010-2019)) and MAGIC-IGAG 2012 were carried out in 2010 and 2012,  
182 respectively. Multichannel and high-resolution seismic reflection profiles, magnetic and swath  
183 bathymetry data were collected during those cruises. A higher resolution magnetic survey was

184 carried out during cruises GEOCAL 2014 and BOLLE 2014 (both in 2014). Structures were  
185 ground truthed with ROV dives in 2014.

### 186 **3.1 High resolution multibeam bathymetry**

187 Bathymetric surveys have been carried out offshore Gaeta Bay from the shelf break to the  
188 Ventotene basin, during cruises MAGIC-IGAG 2012 and BOLLE 2014 with the R/V Urania  
189 using a multibeam Kongsberg EM710 (70-100 kHz,  $1^\circ \times 1^\circ$  along and across track beam width)  
190 characterized by footprint size of 5.3 and 9.5 m<sup>2</sup> at 100 m and 200 m water depth respectively.  
191 Positioning was by differential GPS (accuracy  $\pm 0.4$  m). Sound velocity profiles for acoustic  
192 refraction corrections were derived from multiple Conductivity–Temperature–Depth (CTD) casts  
193 (Seabird 911plus). Multibeam data were processed using Caris Hips and Sips 8.1 software  
194 encompassing: a) corrections for tidal height variations using the Ponza tide gauge ([www.mareo](http://www.mareo)  
195 [grafico.it](http://grafico.it)), b) multibeam transducers calibration using survey patch tests, c) statistical and  
196 geometrical (angle and distance) filters to remove coherent and incoherent noise in each swath,  
197 d) manual removal of isolated fake soundings (Bosman et al, 2015). Bathymetric data were  
198 gridded to produce a series of high-resolution bathymetric maps with cell sizes varying from 1 to  
199 5 m (Fig. 2). Multibeam backscatter data were processed using SIPS SST (Side Scan Tools),  
200 including radiometric and geometric corrections and mosaicking (Micallef et al, 2012). The  
201 backscatter data were exported as a 32-bit raster image with cell size of 5 m.

### 202 **3.2 Multichannel seismic profile TIR10-17**

203 The Seismic line TIR10-17 (Fig. 3) was acquired during the TIR-10 cruise. A tuned array of  
204 three SERCEL's GI-GUNs, configured in harmonic mode (60+60 in<sup>3</sup>, 60+60 in<sup>3</sup>, 45+45 in<sup>3</sup>) was  
205 used as seismic source, with an operative pressure of 2000 psi (140 bar) and towed at 5 m. A  
206 1225 m long SERCEL digital seismic streamer towed at a depth of 4-7 m, with 96 channels and

207 12.5 m group interval was employed. Recording length was set at 12 s with a sampling rate of  
208 0.5 ms, shot interval of 37.5 m allowing a 16 common mid-point fold.

209 The industrial package 2D ProMax by Halliburton has been used to process the seismic line  
210 TIR10-17 (SEG D format) in order to generate a post-stack time migrated section ready for  
211 interpretation. The processing sequence (Yilmaz, 2001) consists in several phases. In the pre-  
212 processing phase, field geometry was assigned to the seismic trace in order to store coordinates  
213 of shot and receiver locations on the trace headers; then, trace kill was applied to delete noisy  
214 traces and top mute was used to remove noise above the first arrival and direct waves. A low-  
215 frequency band-limited noise-suppression filter was applied in order to suppress the strong swell  
216 noise affecting the data, followed by a gain recovery function to compensate the spherical  
217 divergence effect. Predictive deconvolution was applied to improve the temporal resolution of  
218 the data and to attenuate multiple reflections. Once the traces were sorted on common mid-point  
219 gathers, a velocity analysis with the constant velocity scan method was carried out in order to  
220 apply the normal move out correction and to produce the first stacked seismic section. A second  
221 velocity analysis was carried out with the semblance method, and the velocity field obtained,  
222 after smoothing, was used to produce the final stack section. Post stack migration algorithms  
223 were used/tested; among all, post stack Kirchhoff migration resulted to be the most efficient.  
224 Finally, other processing steps (radon velocity analysis, tau-p transform, F-K filter) were applied,  
225 in order to improve the signal/noise ratio,

### 226 **3.3 Single-channel seismic profiles**

227 High-resolution seismic stratigraphy is based on sub-bottom profiles spaced about 1 km and  
228 oriented mainly E-W and NW-SE (cruises TIR-10, MAGIC-IGAG 2012, and BOLLE 2014,  
229 Figs. 1, 2, 4, 5). Sub-bottom profiles were acquired using a frequency-modulated source (*chirp*),  
230 operating in the frequency range of 2-7 kHz (Benthos Chirp III) and recorded with a 0.5-0.8 s

231 record section length. Maximum sub-bottom penetration is 50-60 m, vertical resolution measured  
232 on seismic profiles is about 0.5 m. The Chirp lines were processed by GeoSuite All Works  
233 software, applying time varied gain and a band-pass filter. Thicknesses and depths in seismic  
234 profiles are described in two-way travel time (TWT); a seismic velocity of 1500 m/s was used to  
235 convert two-way travel time to depth. Seismic data interpretation was carried out through the  
236 Kingdom Suite software also integrating the bathymetric data.

### 237 **3.4 Magnetic Data**

238 Magnetic data were collected during surveys in the 2010, and 2014. Two regional lines (oriented  
239 about N120° and N30°, respectively) were acquired during the TIR-10 cruise, three lines (two  
240 about N120° and one tie line about N30°) during the GEOCAL 2014 cruise, and five lines (four  
241 about N120° and one tie line about N30°) during the BOLLE 2014 cruise. In total, the study area  
242 was investigated with more than 30000 magnetic measurements along 120 km of parallel and  
243 cross lines (Fig. 6a). Ship-borne magnetic data were acquired by using a Marine Magnetics  
244 SeaSpy marine magnetometer towed 180 m astern of the vessel operated at 1 Hz, resulting in a  
245 ~4 m spatial sampling. The locations of magnetic measurements were calculated from the GPS-  
246 navigated vessel positions using lay-back corrections.

247 Raw data were processed by removing spikes and diurnal corrections were made by making use  
248 of the INGV reference stations of Duronia and L'Aquila. Total field magnetic anomalies were  
249 then calculated by removing the International Geomagnetic Reference Field (11th generation;  
250 <http://www.ngdc.noaa.gov/IAGA/vmod>).

251 The remaining artifacts (i.e. non-systematic errors) in magnetic data have been removed by  
252 applying a leveling procedure by means cross over errors estimation among various tie lines and  
253 regular survey lines. The data have been reduced to the Magnetic North Pole (Fig. 6b), applying

254 a FFT-phase shifting transformation using local inclination ( $57.1^\circ$ ) and declination values ( $2.7^\circ$ )  
255 of the Earth's Magnetic field.

256

### 257 **3.5 ROV dives**

258 Remotely Operated Vehicle (ROV) dives were conducted with the ROV 'Pollux' (Global  
259 Electric Italiana) aboard the R/V Astrea of the Istituto Superiore per la Protezione e la Ricerca  
260 Ambientale (ISPRA). The ROV is equipped with a digital camera (Canon EOS 550D, 20 mega-  
261 pixels), and two underwater strobes (Canon Speedlite 270EX). Three laser beams separated by  
262 10 cm provide scale for photos. Positioning is provided by a depth sensor, a compass and an  
263 underwater acoustic tracking position system (Tracklink 1500 MA, LinkQuest). The ROV dives  
264 (Figs. 2, 7) were planned on the basis of seafloor morphology and the magnetic pattern.

## 265 **4 Results**

### 266 **4.1 Morphology of the Ventotene Volcanic Ridge**

267 The Ventotene Volcanic Ridge (VR) is an 11 km-long NW-SE elongated structure located in the  
268 Gaeta bay close to the shelf break of the Latium-Campanian continental shelf at water depth  
269 ranging between 165 and 400 m (Figs. 1 and 2a). The VR is composed of four morphological  
270 highs (named A, B, C1, C2 in Fig. 2) separated by deep channels. It rises about 200 m from the  
271 surrounding seafloor (yellow dashed lines in Fig. 2a)

272 At local scale, the overall morphology is quite regular, except for the occurrence of craters  
273 produced by emission of fluids from the seabed (i.e. pockmarks), channels and a few small rocky  
274 outcrops located on the summit of the VR (edifices A and B, Fig. 2), suggested by high

275 backscatter intensity (Fig. 2b). The flanks of edifice A and B have high slope gradients on  
276 average (12-20°), decreasing to a few degrees (e.g., Fig. 10) at the base of the ridge (about -400  
277 m). The summit of both edifices is flat and sub-circular or slightly elongated in plan-view; small  
278 rocky outcrops occur on the summit of edifice B. In contrast, the two minor edifices located on  
279 the eastern sector (C1 and C2, Fig. 2), are bounded to the SE by a steep escarpment. Edifice A  
280 rises 200 m from the surrounding seafloor to the south (Fig. 2a), and has a sub-conical shape,  
281 with a basal diameter of 3.5 km flat top with a diameter of 1.5 km, and a summit at 171 m depth.

282 Edifice B (Fig. 2a) is elongated 6.3 km in the NW-SE direction and is 4 km wide. Its summit is  
283 flat and lies at 165 m depth. It also has a sub-conical shape, with a quasi-bilateral symmetry with  
284 respect to a NW-SE axis. The south-eastern flank slopes are steep (18°). Here small ridges  
285 elongated along the slope (edifices C1 and C2, Fig. 2a) are present. These edifices have an  
286 irregular shape and morphology, locally resembling those of edifice A and B. In the eastern  
287 sector, the VR is confined by a well developed escarpment 12 km long, which marks the border  
288 of a deep and wide channel associated up-slope with several gullies (Fig. 2a).

289 The escarpment, the channel and the gullies are oriented roughly in the NE-SW direction.  
290 Several landslide scars occur along the base of the escarpment between 300 and 500 m water  
291 depth. Landslide morphologies are quite complex due to the overlapping of multiple events.  
292 However some primary features can be distinguished, such as headwalls with heights of 10 m  
293 and slope gradients ranging between 28° and 44°.

294 Along the NE-SW escarpment and at the bases of edifices A and B several pockmarks are  
295 present, in particular, a giant depression (i.e., giant pockmark in Fig. 2) toward the east (green  
296 lines, Fig. 2a). The pockmarks have variable size, being 80-300 m wide, 80-1000 m long, and 5-  
297 300 m deep. Most of them are isolated, showing a circular plan-view shape, whereas some of  
298 them are aligned along WSW-ESE and SW-NE directions (Fig. 2). Small pockmarks, having an

299 average diameter of 50 m, circular shape and negative relief of a few meters are present in the  
300 northern part of the VR.

## 301 **4.2 Seismic stratigraphy**

### 302 **4.2.1 Multichannel seismic line TIR10-17**

303 Seismic profile TIR10-17 (Fig. 3) runs in a NW-SE direction for a length of about 37 km and  
304 covers a sector of the continental shelf off Gaeta and the northern border of the upper sector of  
305 the continental slope facing the Ventotene basin, just south of the 200 m isobath. In its  
306 northwestern part, on the continental shelf, the line displays a 1 s-thick (TWT) sedimentary infill,  
307 lying above a highly discontinuous acoustic substratum. In the lowermost part of the basin infill,  
308 reflections are discontinuous and are affected by an extensional or transtensional fault system  
309 that involves the basement. The upper seismic reflections are continuous and parallel, they  
310 display a prograding geometry in the uppermost part and are not involved in the extensional  
311 deformation. Moving along to shot point (SP) 290, the seismic line crosses along the edge of  
312 edifice A (Fig. 2), with a flat summit at <200 ms (TWT). On the western flank of this feature no  
313 faults are observed, while seafloor is deformed and reflections below are folded, suggesting a  
314 volcanic rather than structural origin. Well stratified contourites cover the lower part of the  
315 flanks of this sub-circular cone, and a ring-like erosional channel originated by bottom current  
316 activity surrounds it.

317 The eastern flank of the cone-shaped structure is in contrast affected by normal faulting, which  
318 involves the entire basement, which is only at 0.5 s TWT. This morpho-structural high zone  
319 (between SP 340 and 580) is characterized by a strongly deformed basement overlain by thin  
320 sediment layers; forming small basins, often bounded by tilted blocks, that display strong  
321 wedging and strata growth. Basement structures are poorly imaged.

322 At SP 584 the seismic line crosses a major normal fault trending SW-NE, which offsets the  
323 basement by **over 1.2 s, TWT**, and displays a relict prograding wedge at its hangingwall. This  
324 master fault bounds to the NW the Ventotene basin, producing the SW-NE escarpment shown by  
325 the multibeam bathymetry (Fig. 2a). In this sector, the basin is a gentle syncline, with the  
326 basement rising toward the SE and dissected by extensional faults, especially at the eastern  
327 margins of the basin, where tilted faulted blocks are displayed. The infilling succession is  
328 composed of mostly continuous, from high to low amplitudes, parallel or sub-parallel reflections.  
329 The lowermost seismic unit with a wedge geometry thinning to the SE on the basement highs  
330 may be syn-tectonic. In the south-eastern sector, some incipient faulting affects the upper part of  
331 the sequence, as faults with little or no offsets reach the seafloor.

#### 332 **4.2.2 High resolution sub-bottom profiles**

333 The analysis of the seismic grid covering the VR allows us to recognize the seismic structure of  
334 the shallow subsurface along the main morphological features (edifice A, edifice B and NE-SW  
335 escarpment). Figs. 4, 5 show a series of representative chirp profiles selected across these  
336 morpho-structures. Edifices A and B are imaged along profiles 66, 165, V212 and TIR10-17 (see  
337 Figs. 1,2 for location), These data show three different deposits resting on basement over the  
338 summits. The most recent deposit is a thin (a few meter thick) aggrading deposit (H in Figs. 4b,  
339 4c, and 5b) characterized by high amplitude reflections. Below H a wedge-shaped prograding  
340 deposit is present (W1 in Figs. 4b, 4c, and 4d), that pinches out toward the shelf-edge, is present.  
341 W1 has a depositional edge located at a depth between 180 and 210 m, reaching a max thickness  
342 of about 30 m. H and W1 are separated by a high-amplitude and high continuity reflection (R1).  
343 Possible truncation of underlying reflections suggests that R1 is an erosional unconformity. R1 is  
344 a seaward dipping reflection, and it loses the erosive character (becomes conformable) towards  
345 the basin (Fig 4c), where it is draped by a thin sediment cover (about max. 12 m thick). On the

346 summit of edifice A, another wedge-shaped prograding deposit (W2 in Fig. 4c), about 40 m  
347 thick, is present below W1. Wedges W1 and W2 are separated by reflection R2 (R2 in Fig. 4b  
348 and 4c).

349 The structure of the NE-SW escarpment is imaged by profiles 66 (Fig 4a) and 165 (Fig. 5).  
350 These profiles show the occurrence of well-stratified and deformed deposits (wavy reflections)  
351 with some disrupted reflections. Tilting of strata along the SE sector of the escarpment possibly  
352 suggest recent deformation by faulting. In some cases high-amplitude and high-continuity  
353 reflections having erosive characters are present. Profile 107 (Fig. 5c) crosses the escarpment at  
354 its center, where the escarpment is steep and has a flat summit. The Chirp data from there show  
355 prolonged bottom echoes with no sub-bottoms and some acoustic hyperbolae. These suggest the  
356 presence of rock outcrops or lithified sediments. The apparent curved shapes of reflections  
357 suggest the occurrence of ductile deformation of marine strata with possible faults in the shallow  
358 subsurface.

### 359 **4.3 Magnetics**

360 Magnetic anomaly map (Fig. 6a) shows a complex pattern, with values ranging from about -170  
361 nT up to +330 nT. Magnetic maxima occur on the south side of edifice A (from 0 nT to about  
362 +70 nT), on the east slope of edifice B (up to +65 nT), with the highest anomaly (more than  
363 +300 nT) located at SW-NE escarpment (Fig. 6a).

364 The northern area shows magnetic minimum values, of down to -170 nT. In the Reduced To Pole  
365 (RTP) map (Fig. 6b) the general pattern of the anomalies is maintained, with maximum values in  
366 the south separated from minimum values in the north. Edifices A and B are overlapped by  
367 positive anomalies, and two maxima are approximately centered on the edifice A and in the  
368 eastern flank of the edifice B. The maximum value of the magnetic anomaly is recorded again

369 along the morphologic escarpment. RTP transformation makes a shift of the anomaly so that its  
370 center lies exactly over the steepest bathymetric gradient (Fig. 6b). In general, RTP maxima  
371 indicates the position of the center of the magnetic sources. The direct relationship between RTP  
372 high and steepest gradient may suggest high-magnetized rocks, which crop out along the edifice  
373 flank. The limited extent of the survey does not allow to establish the causes of the transition  
374 from maximum anomalies in the south to minimum anomalies in the north, although the regional  
375 trend may contribute.

#### 376 **4.4 ROV visual inspections**

377 The ROV stations were located on the SW-NE escarpment, at depths of 250 to 415 m, crossing  
378 one of the steepest (up to 45°) sector of the SW-NE escarpment and on its summit.

379 Images from the upper part of the escarpment, (RD1 and RD2 at depth of 294 and 278 m) in Fig.  
380 7 show sub-rounded, dark-colored rocky outcrops characterized by fissures, hollows and bread-  
381 crust features. These outcrops emerge from a sedimentary seafloor and are meter to sub-  
382 meter in size. Their morphologies suggest that they are lava outcrops. A thin sediment cover is  
383 present, thickening toward the base.

384 Images from sites RD3 and RD4, in lower part of the escarpment, at depth of 380 and 417 m  
385 (Fig. 7) show dark-colored rocky outcrops with a rough top surface. These outcrops have metric  
386 size and a more massive appearance than those observed at RD1 and RD2 sites. Overall, their  
387 aspect suggests the occurrence of volcanic rocks. Here, a patchy sediment cover is present on the  
388 outcrops.

389 The ROV visual inspections highlight the presence of rocky seafloor across the escarpment.  
390 There are not available samples collected in the area to be compared with ROV visual  
391 inspection. However, the observed morphologies may be related to lava products, which can be

392 referred to both individual pillows and lava lobes (e.g., Perfit and Soule, 2016, and reference  
393 therein). Pillows extrude as single spherical or cylindrical tubes of lava rimmed by a glassy crust  
394 due to the sea water contact preventing coalescence among adjacent pillows. Pillow flows form  
395 during eruptions with relatively low effusion rates, which gives enough time for a thick crust to  
396 form on all sides of a pillow (Perfit and Soule, 2016). Although the hypothesis of lava pillow can  
397 not be ruled out, the observed rounded outcrops, particularly the hollowed ones, seem to be  
398 better interpreted as a part of lobate flows, which can form during rapid extrusion (e.g., Perfit  
399 and Soule, 2016). Lobate flows generally inflate forming a smooth and flat crust while the lava  
400 remains molten for a time in the flow's interior. This solid crust can later collapse if the lava in  
401 the interior of the flow drains away or may break due to new magma pulses. These processes are  
402 in agreement with the observed morphologies shown in images RD1 and RD2 (Fig. 7).  
403 Individual lobes of lava may quickly coalesce back together into one interconnected flow.

## 404 **5 Interpretation and Discussion**

### 405 **5.1 The Ventotene Volcanic Ridge**

406 Based on the combined information derived from the datasets above, we interpret these edifices  
407 as forming one volcanic structure, the Ventotene Volcanic Ridge complex. Morphological,  
408 geological and geophysical evidences of its volcanic nature are presented here for the first time,  
409 and should be placed within the framework of the eastern Tyrrhenian margin evolution. The  
410 Ventotene Volcanic Ridge represents an independent volcanic system, since it occurs far from  
411 the volcanoes of the Pontine Islands and is structurally separated from these edifices. The  
412 occurrence of this volcanic complex will contribute to the knowledge of the evolution of this  
413 continental margin, being the depth of the flat summit of interest concerning the regional  
414 subsidence.

415 New high resolution multibeam bathymetry reveals morphological features characterized by sub-  
416 conical truncated shape and steep slopes, ascribed to volcanic edifices (Fig. 2a). Their  
417 morphology, shape and size are similar to those observed in shallow-intermediate water through  
418 bathymetric surveys around volcanic islands, e.g., at the Aeolian Islands (Casalbore et al, 2014b;  
419 Romagnoli et al, 2013a,b), at the Azores (Quartau et al, 2014; Casalbore et al, 2015; Weiss et al,  
420 2015) and at Vestmannaeyjar Arcipelago, Iceland (Romagnoli and Jakobsson, 2015).

421 The high-resolution bathymetric data allow to estimate partial volumes of the Ventotene Ridge  
422 edifices A, B, C1, and C2, being 0.54, 1.95, 0.21 and 0.08 km<sup>3</sup>, respectively, considering their  
423 foot as shown in Fig. 2a. The four edifices of the VR (i.e., A, B, C1, and C2) reach a total  
424 volume of 2.8 km<sup>3</sup>. These values can be compared proportionally to the Ventotene volcanic  
425 complex, which has a volume estimated at 105 km<sup>3</sup> (surface area: 440 km<sup>2</sup> and elevation from  
426 the seafloor: 720 m, inset in Fig. 9).

427 Seismic facies analysis of the Ventotene Ridge also indicates that the structural high corresponds  
428 to a volcanic structure. According to Milia and Torrente (2000), the "reflection free" style of the  
429 seismic facies in the single channel profile 66 (Fig. 4) suggests the volcanic origin of the edifices  
430 A and B. Moreover, the increasing incoherent noise in the seismic data beneath the Ventotene  
431 Ridge in the profile TIR10-17 (Fig. 3) corresponds to the general description of volcanic bodies  
432 in multichannel seismic profiles, as well as those that Yoon et al (2014) observed in the Sea of  
433 Japan, in order to depict magmatism and tectonic evolution of the back-arc basin. Similar  
434 seismic facies is observed in a nearby multichannel seismic profile TIR10-13 (Conti, 2014)  
435 located across the northern sector of the Ventotene volcanic complex (Fig. 9) with the same  
436 acquisition parameters and processing sequence of line TIR10-17. In addition, volcanic  
437 structures of the Ventotene complex (Fig 9b), emphasized by high-resolution bathymetric data  
438 from Casalbore et al (2014a), can clearly be observed in the profile TIR10-13 (Fig. 9a and 9c).

439 The similar seismic response of the acoustic basement in TIR10-13 and TIR10-17 seismic  
440 profiles strongly supports the volcanic nature of edifices A and B (Fig. 3). Moreover, in the  
441 paper by Weiss et al (2015), the seismic lines crossing submarine minor cones (parasitic  
442 volcanism) in the Azores area, associated with larger edifices (volcanic islands) give us  
443 confidence in our interpretation of the volcanic nature of the VR. The internal reflections  
444 evidenced and related to summit eruptions described by Weiss et al (2015) are similar to the VR  
445 in term of dimension and depth.

446 High resolution seismic profiles show a complex architecture of recent depositional deposits that  
447 obliterate the original volcanic structures. In more detail, taking into account the seismo-  
448 stratigraphic characters, the horizon R1 (Figs. 4, 5) can be interpreted as an erosional surface  
449 formed during the last glacio-eustatic cycle. R1 is the youngest unconformity depicted in the  
450 shallow subsurface of the study area and it is likely related to the latest lowstand phase (the Last  
451 Glacial Maximum, LGM, Marine Isotope Stage 2, age of about 20 ka). The aggrading deposits,  
452 which lie above R1, formed during the postglacial sea-level rise and present-day-Holocene  
453 highstand phase. Further information regarding the age of the volcanic edifices can be obtained  
454 by the deposition of wedges W1 and W2 (Figs. 4, 5). Within the Mediterranean, these wedge-  
455 shaped prograding deposits are locally observed at the shelf-edge and named submerged  
456 depositional terraces (Calanchi et al, 1995; Chiocci and Orlando, 1996), or shelf-margin  
457 prograding deposits (Trincardi and Field, 1991). These deposits have been observed mostly on  
458 narrow and steep shelves, frequently occurring around shallow banks, ridges and volcanic  
459 islands, or along tectonically active margins (Chiocci et al, 2004; Fraccascia et al, 2013;  
460 Martorelli et al, 2014). Moreover, similar prograding wedges were observed close to the study  
461 area, along the western and eastern Pontine Archipelago (Chiocci and Orlando, 1996; Casalbore  
462 et al, 2016). The shelf edge wedges are thought to be formed below the storm-wave base level  
463 (ranging between -10 and -30 m in the Tyrrhenian Sea, Casalbore et al, 2016), during glacio-

464 eustatic sea-level fall and lowstand periods (Martorelli et al, 2014). They formed through a  
465 progressive down-ward shift of the deposit during the sea-level fall; once the eustatic minimum  
466 was reached, the deposits remained relict below the level reached by the eustatic minimum.  
467 Accordingly, the deposition of the most recent wedge observed at the present-day shelf break  
468 (deposit W1) ended around the Last Glacial Maximum (LGM).

469 The depth of the edge of wedge W1 is -180/-170 m which is deeper than the LGM sea-level  
470 stand (about -120 m according to the glacio-hydro-isostatic model of Lambeck et al, 2011), but  
471 similar to average depths observed on subsiding areas located nearby the Ventotene Volcanic  
472 Ridge (down to -160m; Casalbore et al, 2016). However, considering that the deposit formed  
473 below the wave-base level zone, e.g., at about 10-30 m (Hernández Molina et al, 2000), we infer  
474 that the volcanic edifices underwent a post-LGM subsidence of about 20-50 m, resulting in a  
475 subsidence rate ranging between 1.0 and 2.5 mm/yr. Both these values are consistent with  
476 regional subsidence of the Ventotene Basin (Zitellini et al, 1984). The age of deposit W2 might  
477 be tentatively referred to the penultimate major glacio-eustatic minima (i.e., about 190-135 ka  
478 BP; Marine Isotope Stage 6), implying an age >190-135 ka for edifice A.

479 Edifices A and B can be considered as flat-topped cones (Fig. 2a and 10) with flatness values  
480 (radius of flat top divided by radius of base) in the range between 0.55 and 0.63 and very low  
481 aspect ratios (height divided by basal diameter), in the range between 0.05 and 0.07. Submarine  
482 flat-topped cones have been widely documented, both in deep and shallow water (e.g., Clague et  
483 al, 2000; Mitchell et al, 2012, and reference therein). They are associated to different  
484 geodynamic settings (e.g., spreading centers, mid-plate hot spots) and may reflect various styles  
485 of eruptive activity (effusive vs explosive activity) and geological processes (e.g., interplay of  
486 vertical movements and sedimentary processes related to sea level fluctuations and stillstands).  
487 In deep water settings (> -500 m), around the Hawaiian Islands, several monogenetic flat-topped

488 cones that are characterized by very low aspect ratios (some cones have aspect ratios of about  
489 0.04) have morphologies that are rather similar to those observed on or near spreading centers  
490 and from the deep seafloor (Clague et al, 2000). These flat-topped cones are interpreted as  
491 formed by continuously overflowing lava ponds developed during submarine, long-lived, steady,  
492 effusive, point source eruptions of degassed magma on gentle slopes.

493 In contrast, in shallow water (e.g., < 150 m) monogenetic or composite flat-topped cones formed  
494 in the submarine environment are typically truncated cones produced by subaerial and/or  
495 submarine erosion (guyots). However, recently, Mitchell et al (2012) interpreted monogenetic  
496 flat-topped cones with very low H/W ratios (< 0.1), formed at water depth < -300 m off Azores  
497 (east of Pico Island), as originated by forced spreading of erupting columns during explosive  
498 eruptions by the air-water density interface. Some morphological characteristics of edifices A  
499 and B are rather similar to monogenetic edifices observed in deep and shallow water settings by  
500 Clague et al (2000) and Mitchell et al (2012).

501 However, taking into account the water depth, we tend to exclude these formation mechanisms,  
502 as the primary or single mechanisms, which can lead to the formation of our flat summit  
503 morphologies. In fact, even if flatness values and aspect ratios of edifices A and B are rather  
504 similar to those of the submarine flat-topped volcanic cones documented by Clague et al (2000)  
505 around Hawaiian Islands (cones characterized by basal diameter up to 5 km, heights > 300 m and  
506 low aspect ratios: 0.1-0.2, with some values approaching 0.04), the flat cones described in this  
507 study have smaller sizes, Also, they have gentler flanks (slopes < 20-25°, Fig. 10) and their  
508 summit occur in shallow water (< 200 m), where volcanic activity typically produces cones of  
509 volcanoclastic material emitted during explosive eruptions. If compared with the flat cones  
510 described by Mitchell et al (2012), the edifices A and B are bigger (cone width > 2500 m) and  
511 much flatter. Moreover, the elongated shape of edifice B (Fig. 2a and 10b) and possible

512 occurrence of two distinct cones on seismic profile TIR10-17 crossing edifice A (Fig. 4e) would  
513 indicate that both these cones are not monogenetic but originated through multiple eruption  
514 episodes that produced composite edifices.

515 As both the edifices may have erupted before 190-135 ka and their summit is located in shallow  
516 water (present water depth of about 170 m), the most likely mechanism that produced the flat-  
517 topped morphology may be related to erosional processes related to wave action during the LGM  
518 and penultimate marine lowstand period (MIS 6). In fact, as reported above, the volcanic edifices  
519 possibly underwent a post-LGM subsidence of about 30-50 m. Therefore, during the LGM, their  
520 summit was located at about -140/-120 m, within the range of wave-dominated marine processes,  
521 considering a wave erosion depth of about 10-30 m (Casalbore et al, 2016, and references  
522 therein). Evidence of wave-dominated erosional processes occurred during lowstand periods is  
523 provided by the erosive character of horizons R1, R2 (Fig. 4). This hypothesis is sustained by  
524 occurrence of wedges W1 and W2 that can be interpreted as submerged depositional terraces,  
525 formed below the lowstand sea level under the influence of wave processes (see discussion  
526 above).

527 Marine erosion by surf produced the flat summit morphologies. However, the deposition of  
528 wedges W1 and W2 also produced the enlargement of their summit and thus increased their  
529 flattening values. In this context, the observed flat-topped morphologies likely originated by both  
530 erosive and depositional marine processes related to wave action. In this regard, the proposed  
531 mechanism is quite similar to what proposed by Romagnoli and Jakobsson (2015) for the Surtsey  
532 complex, in the Vestmannaeyjar archipelago. There, major morphological changes due to wave  
533 processes occurred along the shallow water portions of the Surtsey complex (Surtsey and its  
534 satellite vents), after the 1963-1967 Surtseyan eruption. These changes were related to a mixed  
535 contribution of wave-dominated erosional and depositional processes, which contributed to the

536 enlargement of shelf sectors. Therefore, we consider that the origin of the observed  
537 morphologies differs from the mechanisms proposed by Clague et al (2000) and Mitchell et al  
538 (2012), reflecting more a post-eruptive evolution than a primary volcanic processes. This  
539 mechanism highlights that also wave-dominated depositional processes can represent a relevant  
540 factor for re-shaping and widening of shelves surrounding Pleistocene volcanic edifices.

541 As edifices A and B are located in shallow water, we consider that explosive activity, owing to  
542 decreased confining pressure and the expansion of seawater, may represent a relevant  
543 mechanism for their growth. Unfortunately, the accurate definition of eruption style is prevented  
544 at present, due to the lack of petrological and geochemical data of rock samples, as well as due to  
545 the impossibility to clearly observe primary volcanic landforms (e.g., craters, lava flows, domes,  
546 etc.), even analyzing multibeam bathymetric data at maximum resolution (slope map in Fig.  
547 10b), as they are masked by sediment cover and erosional processes.

## 548 **5.1 The Ventotene Volcanic Ridge in the tectonic context of the central-** 549 **eastern Tyrrhenian Sea**

550 Several volcanic edifices as a result of the Plio-Pleistocene extensional tectonics characterize the  
551 central-eastern Tyrrhenian Sea.

552 The magnetic data here presented are compatible with the presence of a widespread and  
553 scattered volcanism, comparable to same analogues previously described in Tyrrhenian Sea (i.e.  
554 the Palinuro seamount, Caratori Tontini et al, 2009; Ligi et al, 2014). Given that the new ship-  
555 borne magnetic data suggest possible volcanic structures, a regional view of the magnetic  
556 anomaly pattern may help in the interpretation. Thus, the regional magnetic anomaly of the  
557 Pontine region has been extracted from the Aeromagnetic Map of Italy (Caratori Tontini et al,  
558 2004), reprocessed and reduced to the magnetic pole. The reduce-to-pole regional map (Fig. 8)

559 shows a complex pattern of the anomalies. Local, high frequency magnetic anomalies have been  
560 ascribed to the presence of a subaerial volcanic edifice (Bruno et al, 2002; de Alteriis et al, 2006)  
561 and to the occurrence of volcanoclastic sediments reworked from the continental shelf (Aiello et  
562 al, 2011). Volcanic complexes in the region correlate with magnetic anomaly maxima, i.e., the  
563 Ventotene-Santo Stefano area (about 140 nT), and the Ischia-Procida offshore (>400 nT),  
564 whereas poor correlation exists with the Ponza-Palmarola volcanic complexes. In the study area,  
565 a large E-W aligned positive anomaly is clearly observable in correspondence of the VR and its  
566 eastern extension along the 41°N parallel (de Alteriis et al., 2006) with amplitude and frequency  
567 content comparable with those of the Ischia and Procida volcanoes, suggesting that the VR may  
568 be part of a larger volcanic system extending eastward (Fig. 8).

569 The occurrence of volcanic activity in the study area may be related to extension in back-arc  
570 basins, associated to subduction zone dynamics. In fact extensional deformation often develops  
571 through several interacting systems of normal faults, in which volcanism can sometimes take  
572 place along many directions of extension (Carminati et al, 2010; Aitken et al, 2011; Yoon et al,  
573 2014). Some authors describe volcanism at regional scale localized along the main direction of  
574 extension (e.g., the tectono-magmatic provinces along the Main Ethiopian Rift, Ebinger and  
575 Casey, 2001; Muluneh et al, 2014) as well as others indicate that volcanism along rifted margin  
576 can also take place along transfer faults with respect to the normal fault distribution (Acocella  
577 and Funiciello, 2006, and references therein).

578 The studied sector of the Tyrrhenian back-arc basin presents a complex distribution of normal  
579 faults and volcanoes (e.g., Carminati et al, 2010, and references therein). The structural map of  
580 the main basal unconformity obtained by Conti (2014) with the integration of different  
581 multichannel seismic databases (Fig. 11), provides the principal directions of the normal fault  
582 systems in the Gaeta Bay, and shows the spatial relationships between extensional deformations

583 and volcanic complexes. The surface in Fig. 11 is two-way time (TWT, ms) structural map of the  
584 main basal unconformity (black line in Fig. 3, top Messinian?) and displays the structural setting  
585 of the substrate on which the whole postorogenic sequence is deposited. The surface is affected  
586 by several major normal faults forming alternation of structural highs and depressions.  
587 Preferential structural directions are NNE-SSW on the western part and WNW-ESE in the  
588 eastern part of the investigated area.

589 The Ventotene Volcanic Ridge is part of a structural high lined along the 41° parallel regional  
590 magnetic alignment (de Alteriis et al., 2006) and bordered by two ~E-W major opposite normal  
591 faults, with the southernmost bounding the Ventotene basin to the north (Fig. 11). Although the  
592 alignment of the top of the volcanic edifice follows a NW-SE trend (Fig. 2a), compatible to the  
593 extensional setting of the Tyrrhenian domain (e.g., Carminati et al, 2010, and references therein),  
594 we interpret these volcanic edifices to have arisen by eruption above a NE-SW transfer fault or  
595 zone between the NW-SE rift-related normal faults. In fact, several NE-SW trending lineaments  
596 affects the study area (Figs 2a and. 3), clear NE-SW trending scarps or narrow depressions are  
597 visible in C1 and C2, respectively, as well as a minor NE-SW lineament also appears between  
598 edifices A and B. Although we do not have other lines of evidence, it is worth to note that a very  
599 well developed NE- SW normal fault system is present in this sector of the Tyrrhenian margin  
600 (Acocella and Funiciello, 2006) shaping the escarpment southeast of Ponza and Palmarola  
601 islands. The island of Ponza is built along a NE-SW fissure system (De Rita et al, 2001);  
602 following this evidence, NE- SW lineaments at the VR can be considered as eruptive fissures, as  
603 also indicated by ROV visual inspections. Transverse systems, with oblique strike respect to the  
604 main set of extensional faults, can occur in extensional settings, also associated to active  
605 volcanic activity, as for example in the subaerial analogue of the Tarawera eruptive fissure,  
606 formed in 1886 in Okataina caldera (New Zealand) (Acocella et al, 2003; Seebeck et al, 2010).

607 In the case of the Ventotene Volcanic Ridge, while the overall alignment of these volcanoes is  
608 NW-SE, there could be an evidence for orthogonal volcanic activity.

## 609 **6 Conclusions**

610 Results from this study highlight that the analysis of volcanic morpho-bathymetric elements  
611 located in shallow-intermediate water depths takes particular advantage of the use of very high  
612 resolution techniques (e.g., multibeam bathymetry and seismic profiles), high-density surveys  
613 (e.g., magnetic survey) and full coverage of the seafloor bathymetry.

614 The **new exploration of the** Ventotene Volcanic Ridge contributes to the knowledge of the  
615 evolution of the Pleistocene volcanism off the Gaeta Bay along the Latium–Campanian margin.  
616 **This paper shows the volcanic origin of the Ventotene Ridge, adding to the number of known**  
617 **volcanic** edifices in the central-eastern Tyrrhenian Sea. It constitutes an additional partially-  
618 buried volcanic structure possibly coeval with Ventotene Island, **formed by** Tyrrhenian back-arc  
619 basin magmatism.

620 In the central-eastern area of the Tyrrhenian Sea there is a well-defined alignment of volcanoes  
621 from NW to SE, from Ponza to Ischia, passing through Ventotene (Fig. 1). This alignment is  
622 compatible with the evolution and the NE-SW migration of the Apennines thrust front in that  
623 region and the tensional tectonics in the backarc **Tyrrhenian basin of the Apennines subduction**.  
624 Location of Ventotene Volcanic Ridge extends the **known** Pontine volcanism landward.  
625 **Although main volcanic edifices of this volcanic complex develop along the NW-SE direction, it**  
626 **belongs to** a regional E-W volcanic alignment as far as Parete Volcano **on land** (Fig. 1). **In turn,**  
627 **it** lies between a NE-SW trending graben to the southwest of the Roccamonfina volcano  
628 **(Acocella and Funicciello, 2002; Acocella and Funicciello, 2006; Vignaroli et al, 2016)**, on the one  
629 side, and a major NE-SW trending escarpment to the east of Ponza, on the other side. **Complexly**

630 **distributed** normal and/or transtensional faults in the area (Fig. 11), likely drove the volcanic  
631 activity, **which produced** the Ventotene Volcanic Ridge. Thus, we argue that this volcanic  
632 complex **developed** due to transtensional deformation along a NE-SW fault **system as** a transfer  
633 zone between the segmented NW-SE rift-related normal faults, during the evolution of the  
634 Tyrrhenian back-arc basins.

## 635 **Acknowledgments**

636 During the first revision of this article, Giovanni Bortoluzzi passed away. Giovanni has been an  
637 essential mentor for us during these years. We are very grateful to him for his initiative to  
638 improve collaborative research among scientists involved in different topics of marine geology,  
639 and for the several cruises he organized and led in the Mediterranean Sea and the oceans. We  
640 will miss his curiosity, his generosity, and his enthusiasm for the sea, science and exploration.  
641 The officers and the crew of the R/V Urania and R/V Astrea, and the scientific party of the TIR-  
642 10, MAGIC-IGAG 2012, GEOCAL 2014, and BOLLE 2014 surveys are thanked for their  
643 cooperation during fieldwork. Prof. Marzia Bo from the University of Genova is warmly  
644 acknowledged for the use of R/V Astrea during her cruise ECOSAFIMED on August 2014.  
645 Discussions with A. Billi were much appreciated. The article strongly benefited from the reviews  
646 by J. D. L. White, V. Acocella, N. C. Mitchell and G. de Alteriis. This research was partially  
647 supported by the Consiglio Nazionale delle Ricerche (CNR) of Italy under the sponsorship of  
648 Dipartimento Terra Ambiente (cruise TIR-10).

## 649 **References**

650 Acocella V, Funiciello R (2002) Transverse structures and volcanic activity along the  
651 Tyrrhenian margin of central Italy. *Boll Soc Geol Italiana* 1:739–747.

652 Acocella V, Funicello R (2006) Transverse systems along the extensional Tyrrhenian margin  
653 of central Italy and their influence on volcanism. *Tectonics* 25,  
654 DOI:10.1029/2005TC0018455

655 Acocella V, Spinks K, Cole J, Nicol A (2003) Oblique back arc rifting of Taupo Volcanic  
656 Zone, New Zealand. *Tectonics* 4, DOI:10.1029/2002TC001447,

657 Aiello G, Cicchella AG, Di Fiore V, Marsella E (2011) New seismo-stratigraphic data of the  
658 Volturno Basin (northern Campania, Tyrrhenian margin, southern Italy): implications for  
659 tectono-stratigraphy of the Campania and Latium sedimentary basins. *Ann Geophys* 54,  
660 DOI:10.4401/ag-4777

661 Aitken T, Mann P, Escalona A, Christeson GL (2011) Evolution of the Grenada and Tobago  
662 basins and implications for arc migration. *Mar Petr Geol* 28:235–258

663 Alessio M, Bella F, Improta S, Belluomini G, Calderoni G, Cortesi C, Turi B (1974)  
664 University of Rome Carbon-14 dates XII. *Radiocarbon* 16:358–367

665 Argnani A, Savelli S (1999) Cenozoic volcanism and tectonics in the southern Tyrrhenian sea:  
666 space-time distribution and geodynamic significance. *J Geodyn* 27:409–432

667 Arnulf AF, Harding AJ, Kent GM, Carbotte SM, Canales JP, Nedimović MR (2014) Anatomy  
668 of an active submarine volcano. *Geology* 42:655–658

669 Bani P, Normier A, Bacri C, Allard P, Gunawan H, Hendrasto M, Surono M, Tsanev V (2015)  
670 First measurement of the volcanic gas output from Anak Krakatau, Indonesia. *J Volcanol*  
671 *Geotherm Res* 302:237–241

672 Bartole R (1984) Tectonic structure of the Latium-Campanian shelf (Tyrrhenian Sea). *Boll*  
673 *Oceanografia Teorica e Applicata* 2:197–230

674 Beccaluva et al (1990) Geochemistry and mineralogy of volcanic rocks from ODP sites 650,  
675 651, 655, and 654 in the Tyrrhenian Sea. In: Stewart NJ (ed) Proceedings of the Ocean  
676 Drilling Program, Scientific Result, U.S. Gov. Print. Off., 107:49–74

677 Bortoluzzi G, Ligi M, Romagnoli C, Cocchi L, Casalbore D, Sgroi T, Cuffaro M, Caratori  
678 Tontini F, D’Oriano F, Ferrante V, Remia A, Riminucci F (2010) Interactions between  
679 Volcanism and Tectonics in the Western Aeolian Sector, Southern Tyrrhenian Sea.  
680 *Geophys J Int* 183:64–78

681 Bosman A, Chiocci FL, Romagnoli C (2009) Morpho-structural setting of Stromboli volcano  
682 revealed by high-resolution bathymetry and backscatter data of its submarine portions. *Bull*  
683 *Volcanol* 71:1007–1019

684 Bosman A, Casalbore D, Romagnoli C, Chiocci FL (2014) Formation of an “a” a lava delta:  
685 Insights from time-lapse multibeam bathymetry and direct observations during the  
686 Stromboli 2007 eruption. *Bull Volcanol* 76, DOI:10.1007/s00445-014-0838-2

687 Bosman A, Casalbore D, Anzidei M, Muccini F, Carmisciano C, Chiocci FL (2015) The first  
688 ultra-high resolution Digital Terrain Model of the shallow-water sector around Lipari Island  
689 (Aeolian Islands, Italy). *Ann Geophys* 48, DOI:10.4401/ag-6746

690 Bruno PG, de Alteriis G, Florio G (2002) The western undersea section of the Ischia volcanic  
691 complex (Italy, Tyrrhenian sea) inferred by marine geophysical data. *Geophys Res Lett* 29,  
692 DOI:10.1029/2001GL013904

693 Buttinelli M, Scrocca D, De Rita D, Quattrocchi F (2014) Modes of stepwise eastward  
694 migration of the northern Tyrrhenian Sea back-arc extension: Evidences from the northern  
695 Latium offshore (Italy). *Tectonics* 32, DOI: 10.1002/2013TC003365

696 Cadoux A, Pinti DL, Aznar C, Chiesa S, Gillot P (2005) New chronological and geochemical  
697 constraints on the genesis and geological evolution of Ponza and Palmarola volcanic islands  
698 (Tyrrhenian Sea, Italy). *Lithos* 81:121–151

699 Calanchi N, Colantoni P, Rossi PL, Saitta M, Serri G (1989) The Strait of Sicily continental rift  
700 systems: Physiography and petrochemistry of the submarine volcanic centres. *Mar Geol*  
701 87:55–83

702 Calanchi N, Romagnoli C, Rossi LR (1995) Morphostructural features and some petrochemical  
703 data from the submerged area around Alicudi and Filicudi volcanic islands (Aeolian Arc,  
704 southern Tyrrhenian Sea). *Mar Geol* 123:215–238

705 Calò M, Parisi L (2014) Evidences of a lithospheric fault zone in the Sicily Channel  
706 continental rift (southern Italy) from instrumental seismicity data. *Geophys J Int* 199:219–  
707 225

708 Caratori Tontini F, Stefanelli P, Giori I, Faggioni O, Carmisciano C (2004) The revised  
709 aeromagnetic anomaly map of Italy. *Ann Geophys* 47:1547–1555

710 Caratori Tontini F, Cocchi L, Carmisciano C (2009) Rapid 3-D forward model of potential  
711 fields with application to the Palinuro Seamount magnetic anomaly (southern Tyrrhenian  
712 Sea, Italy). *J Geophys Res* 116, DOI:10.1029/2008JB005907

713 Caratori Tontini F, Cocchi L, Muccini F, Carmisciano C, Marani M, Bonatti E, Ligi M, Boschi  
714 E (2010) Potential-field modeling of collapse-prone submarine volcanoes in the southern  
715 Tyrrhenian Sea (Italy). *Geophys Res Lett* 37, DOI:10.1029/2009GL041757

716 Carminati E, Lustrino M, Cuffaro M, Doglioni C (2010) Tectonics, magmatism and  
717 geodynamics of Italy: what we know and what we imagine. *J Virt Expl* 36:1–62

718 Casalbore D, Bosman A, Martorelli E, Chiocci FL (2014a) Mass Wasting Features on the  
719 Submarine Flanks of Ventotene Volcanic Edifice (Tyrrhenian Sea, Italy). In: Krastel et al  
720 (ed) Submarine Mass Movements and Their Consequences, Advances in Natural and  
721 Technological Hazards Research, Springer Int. Pub., 37:285–293

722 Casalbore D, Bosman A, Romagnoli C, Chiocci FL (2014b) Morphology of Lipari offshore  
723 (Southern Tyrrhenian Sea). J Maps DOI: 10.1080/17445647.2014.980858

724 Casalbore D, Romagnoli C, Pimentel A, Quartau R, Casas D, Ercilla G, Hipólito R, Sposato A,  
725 Chiocci FL (2015) Volcanic, tectonic and mass-wasting processes of offshore Terceira  
726 Island (Azores) revealed by high-resolution seafloor mapping. Bull Volcanol 77, DOI  
727 10.1007/s00445-015-0905-3

728 Casalbore D, Falese F, Martorelli E, Romagnoli C, Chiocci FL (2016) Submarine depositional  
729 terraces in the Tyrrhenian Sea as a proxy for paleo-sea level reconstruction: Problems and  
730 perspective. Quaternary Int, In press

731 Catalano S, Tortorici L, Viccaro M (2014) Regional tectonic control on large size explosive  
732 eruptions: Insights into the green tuff ignimbrite unit of pantelleria. J Geodyn 73:23–33

733 Chiocci FL, Martorelli E (2015) Note illustrative e Carta Geologica in scala 1:50.000 delle aree  
734 maine del Foglio 413 Borgo Grappa, ISPRA. Carta Geologica d'Italia. (in press).

735 Chiocci FL, Orlando L (1996) Lowstand terraces on Tyrrhenian Sea steep continental slopes.  
736 Mar Geol 134:127–143

737 Chiocci FL, D'Angelo S, Romagnoli C, Ricci Lucchi F (2004) Terrazzi deposizionali  
738 sommersi lungo le coste italiane. In: Chiocci FL, D'Angelo S, Romagnoli C (eds) Atlante  
739 dei terrazzi deposizionali sommersi lungo le coste italiane, Memorie Descrittive della Carta  
740 Geologica d'Italia, 58:187–194

741 Clague D, Moore J, Reynolds J (2000) Formation of flat-topped volcanic cones in Hawaii. Bull  
742 Volcanol 62:214–233

743 Conte AM, Dolfi D (2002) Petrological and geochemical characteristics of Plio-Pleistocene  
744 Volcanics from Ponza Island (Tyrrhenian Sea, Italy). Mineral Petrol 74:75–94

745 Conte AM, Martorelli E, Calarco M, Sposato A, Perinelli C, Coltelli M, Chiocci FL (2014)  
746 The 1891 submarine eruption offshore Pantelleria Island (Sicily Channel, Italy):  
747 Identification of the vent and characterization of products and eruptive style. Geochem  
748 Geophys Geosystems 15:2555–2574

749 Conte AM, Perinelli C, Bianchini G, Natale C, Martorelli E, Chiocci FL (2016) New insights  
750 on the petrology of submarine volcanics from the western pontine archipelago (tyrrhenian  
751 sea, italy). J Volcanol Geotherm Res, <http://dx.doi.org/10.1016/j.jvolgeores.2016.08.005>, in  
752 press

753 Conti A (2014) Processing and interpretation of new multichannel seismic profiles. The  
754 Central-Eastern margin of the Tyrrhenian basin, *PhD Thesis*, Sapienza Universit\_ di Roma,  
755 Rome, Italy

756 Day S, Llanes P, Silver E, Hoffmann G, Ward S, Driscoll N (2015) Submarine landslide  
757 deposits of the historical lateral collapse of Ritter Island, Papua New Guinea. Mar Pet Geol  
758 67:419–438

759 de Alteriis G, Fedi M, Passaro S, Siniscalchi A (2006) Magneto-seismic interpretation of  
760 subsurface volcanism in the Gaeta Gulf (Italy, Tyrrhenian Sea). Ann Geophys 49:929–943

761 De Rita D, Funicello R, Pantosti D, Salvini F, Sposato A, Velona' M (1986) Geological and  
762 structural characteristics of the Pontine Islands (Italy). Mem Soc Geol It 36:55–67

763 De Rita D, Giordano G, Cecili A (2001) A model for submarine rhyolite dome growth: Ponza  
764 Island (central Italy). *J Volcanol Geotherm Res* 187:221–239

765 Dekov VM, Savelli C (2004) Hydrothermal activity in the SE Tyrrhenian Sea: An overview of  
766 30 years of research. *Mar Geol* 204:161–185

767 Doglioni C (1991) A proposal of kinematic modelling for W-dipping subductions - Possible  
768 applications to the Tyrrhenian-Apennines system. *Terra Nova* 3:423–434

769 Doglioni C, Merlini S, Cantarella G (1999) Foredeep geometries at the front of the Apennines  
770 in the Ionian sea (central Mediterranean). *Earth Planet Sci Lett* 168:243–254

771 Doglioni C, Innocenti F, Morellato C, Procaccianti D, Scrocca D (2004) On the Tyrrhenian Sea  
772 opening. *Mem Descr Carta Geol d'Italia* 44:147–164

773 Ebinger C, Casey M (2001) Continental breakup in magmatic province: An Ethiopian example.  
774 *Geology* 29:527–530

775 Faccenna C, Mattei M, Funiciello R, Jolivet L (1997) Styles of back-arc extension in the  
776 Central Mediterranean. *Terra Nova* 9:126–130

777 Fraccascia S, Chiocci FL, Scrocca D, Falese F (2013) Very high-resolution seismic  
778 stratigraphy of Pleistocene eustatic minima markers as a tool to reconstruct the tectonic  
779 evolution of the northern Latium shelf (Tyrrhenian Sea, Italy). *Geology* 41:375–378

780 Gruen G, Weis P, Driesner T, Heinrich CA, de Ronde CEJ (2014) Hydrodynamic modeling of  
781 magmatic-hydrothermal activity at submarine arc volcanoes, with implications for ore  
782 formation. *Earth Planet Sci Lett* 404:307–318

783 Hernández Molina FJ, Fernández-Salas LM, Lobo F, Somoza L, Díaz-del-Río V, Alverinho  
784 Dias JM (2000) The infralittoral prograding wedge: a new large-scale progradational  
785 sedimentary body in shallow marine environments. *Geo-Mar Lett* 20:109–117

786 Honscho C, Ura T, Asada A, Kim K, Nagahashi K (2015) High-resolution acoustic mapping to  
787 understand the ore deposit in the Bayonnaise knoll caldera, Izu-Ogasawara arc. *J Geophys*  
788 *Res* 120:2070–2092

789 Iezzi G, Caso C, Ventura G, Vallefucio M, Behrens ACH, Mollo S, Paltrinieri D, Signanini P,  
790 Vetere F (2014) First documented deep submarine explosive eruptions at the Marsili  
791 seamount (Tyrrhenian Sea, Italy): A case of historical volcanism in the Mediterranean sea.  
792 *Gondwana Res* 25:764–774

793 Ingrassia M, Martorelli E, Bosman A, Macelloni L, Sposato A, Chiocci FL (2015) The  
794 Zannone Giant Pockmark: First evidence of a giant complex seeping structure in shallow-  
795 water, central Mediterranean Sea, Italy. *Mar Geol* 363:38–51

796 Italiano F, De SA, Favali P, Rainone HL, Rusi S, Signanini P (2014) The Marsili Volcanic  
797 Seamount (Southern Tyrrhenian Sea): A potential offshore geothermal resource. *Energies*  
798 7:4068–4086

799 Kastens et al (1988) ODP Leg 107 in the Tyrrhenian Sea: Insights into passive margin and  
800 back-arc basin evolution. *Geol Soc Am Bull* 100:1140–1156

801 Lambeck K, Antonioli F, Anzidei M, Ferranti L, Leoni G, Scicchitano G, Silenzi S (2011) Sea  
802 level change along the Italian coast during the Holocene and projections for the future.  
803 *Quaternary Int* 232:250–257

804 Ligi M, Cocchi L, Bortoluzzi G, D’Orlando F, Muccini F, Caratori Tontini F, de Ronde CE,  
805 Carmisciano C (2014) Mapping of seafloor hydrothermally altered rocks using geophysical  
806 methods: Marsili and Palinuro seamounts, southern Tyrrhenian Sea. *Econ Geol* 109:103–  
807 2117

808 Loreto MF, Pepe F, De RR, Ventura G, Ferrante V, Speranza F, Tomini I, Sacchi M (2015)  
809 Geophysical investigation of Pleistocene volcanism and tectonics offshore Capo Vaticano  
810 (Calabria, southeastern Tyrrhenian Sea). *J Geodyn* 99:71–86

811 Malinverno A, Ryan WBF (1986) Extension in the Tyrrhenian Sea and shortening in the  
812 Apennines as a result of arc migration driven by sinking of the lithosphere. *Tectonics*  
813 5:227–245

814 Marani MP, Gamberi F (2004) Structural framework of the Tyrrhenian Sea unveiled by  
815 seafloor morphology. In: Marani MP, Gamberi F, Bonatti E (eds) *From Seafloor to Deep*  
816 *Mantle: Architecture of the Tyrrhenian Backarc Basin*, Mem Descr Carta Geol d'Italia,  
817 44:97–108

818 Martorelli E, Falese F, Chiocci FL (2014) Overview of late quaternary continental shelf  
819 deposits off Italian peninsula. In: Chiocci FL, Chivas AAR (eds) *Continental Shelves of the*  
820 *World. Their Evolution During the last Glacio-eustatic cycle*, Geological Society Memoir,  
821 41:171–186

822 Mauffret A, Contrucci I, Brunet C (1999) Structural evolution of the Northern Tyrrhenian Sea  
823 from new seismic data. *Mar Petrol Geol* 16:381–407

824 Metrich N, Santacroce R, Savelli C (1988) Ventotene, a potassic Quaternary volcano in central  
825 Tyrrhenian Sea. *Rend Soc It Min Petr* 43:1195–1213

826 Micallef A, Le Bas T, Huvenne AAI, Blondel P, Huhnerbach V, Deidun A (2012) A multi-  
827 method approach for benthic habitat mapping of shallow coastal areas with high-resolution  
828 multibeam data. *Cont Shelf Res* 1:4–26

- 829 Milia A, Torrente MM (2000) Fold uplift and synkinematic stratal architectures in a region of  
830 active transtensional tectonics and volcanism, eastern Tyrrhenian Sea. *Geol Soc Am Bull*  
831 112:1531–1542
- 832 Mitchell NC, Stretch R, Oppenheimer C, Kay D, Beier C (2012) Cone morphologies  
833 associated with shallow marine eruptions: east Pico Island, Azores. *Bull Volcanol* 74:2289–  
834 2300
- 835 Moeller S, Grevemeyer I, Ranero CR, Berndt C, Klaeschen D, Sallares V, Zitellini N, de  
836 Franco R (2013) Early-stage rifting of the northern Tyrrhenian Sea Basin: Results from a  
837 combined wide-angle and multichannel seismic study. *Geochem Geophys Geosyst*  
838 14:3032–3052
- 839 Muluneh AA, Cuffaro M, Doglioni C (2014) Left-lateral transtension along the Ethiopian Rift  
840 and constrains on the mantle-reference plate motions. *Tectonophysics* 632:21–31
- 841 Palano M, Ferranti L, Monaco C, Mattia M, Aloisi M, Bruno V, Cannav\_ F, Siligato G (2012)  
842 GPS velocity and strain fields in Sicily and southern Calabria, Italy: Updated geodetic  
843 constraints on tectonic block interaction in the central Mediterranean. *J Geophys Res* 117,  
844 DOI:10.1029/2012JB009254
- 845 Patacca E, Sartori R, Scandone P (1992) Tyrrhenian basin and Apenninic arcs: kinematic  
846 relations since Late Tortonian times. *Mem Soc Geol Ital* 45:425–451
- 847 Peccerillo A (2005) Plio–Quaternary Volcanism in Italy: Petrology, Geochemistry,  
848 Geodynamics. Springer-Verlag, Berlin
- 849 Perfit MR, Soule SA (2016) Submarine Lava Types. In: Harff J, Meschede M, Petersen S, Thiede J  
850 (eds) *Encyclopedia of Marine Geosciences*, Springer Netherlands, 808–817

851 Quartau R, Hipòlito R, Romagnoli C, Casalbore D, Madeira J, Tempera F, Roque C, Chiocci  
852 FL (2014) The morphology of insular shelves as a key for understanding the geological  
853 evolution of volcanic islands: Insights from Terceira Island (Azores). *Geochem Geophys*  
854 *Geosys* 15:1801–1826

855 Romagnoli C, Jakobsson SP (2015) Post-eruptive morphological evolution of island volcanoes:  
856 Surtsey as a modern case study. *Geomorphology* 250:384–396

857 Romagnoli C, Casalbore D, Bortoluzzi G, Bosman A, Chiocci FL, D’Oriano F, Gamberi F,  
858 Ligi M, Marani M (2013a) Bathy-morphological setting of the Aeolian Islands. In: F Lucchi  
859 and A Peccerillo and J Keller C A Tranne and P L Rossi (ed) *The Aeolian Islands*  
860 *Volcanoes*, Mem. Geol. Soc. London, 37:27–36

861 Romagnoli C, Casalbore D, Bosman A (2013b) Submarine structure of Vulcano volcano  
862 (Aeolian islands) revealed by high-resolution bathymetry and seismo-acoustic data. *Mar*  
863 *Geol* 48:30–45

864 Rosenbaum G, Lister GS (2004) Neogene and Quaternary rollback evolution of the Tyrrhenian  
865 Sea, the Apennines and the Sicilian Maghrebides. *Tectonics* 23,  
866 DOI:10.1029/2003TC001518

867 Rotella MD, Wilson CJN, Barker SJ, Ian SC, Wright IC, Wysoczanski RJ (2015) Dynamics of  
868 deep submarine silicic explosive eruptions in the Kermadec arc, as reflected in pumice  
869 vesicularity textures. *J Volcanol Geotherm Res* 301:314–332

870 Scrocca D, Doglioni C, Innocenti F (2003) Constraints for an interpretation of the Italian  
871 geodynamics: a review. In: Scrocca D, Doglioni C, Innocenti F, Manetti P, Mazzotti A,  
872 Bertelli L, Burbi L, Doffizi S (eds) *CROP Atlas: seismic reflection profiles of the Italian*  
873 *crust*, Mem. Descr. della Carta Geologica d’Italia, 62:15–46

874 Scrocca D, Carminati E, Doglioni C, Procaccianti D (2012) Tyrrhenian Sea. In: Roberts DG,  
875 Bally AW (eds) *Regional Geology and Tectonics: Phanerozoic Passive Margins, Cratonic*  
876 *Basins and Global Tectonic Maps*, Elsevier, 1C:473–485

877 Seebeck H, Nicol A, Stern T, Bibby HM, Stagpoole V (2010) Fault controls on the geometry  
878 and location of the Okataina Caldera, Taupo Volcanic Zone, New Zealand. *J Volcanol*  
879 *Geotherm Res* 190:136–151

880 Serri G, Innocenti F, Manetti P (2001) Magmatism from Mesozoic to Present: petrogenesis  
881 time-space distribution and geodynamic implications. In: Vai GB, Martini IP (eds)  
882 *Anatomy of an Orogen: the Apennines and the adjacent Mediterranean Basins*, Kluw. Acad.  
883 *Pub.*, p 77–104

884 Sibrant ALR, Hildenbrand A, Marques FO, Weiss B, Boulesteix T, H\_bscher C, L\_dmann T,  
885 Costa ACC, Catal\_o JC (2015) Morpho-structural evolution of a volcanic island developed  
886 inside an active oceanic rift: S. Miguel Island (Terceira Rift, Azores). *J Volcanol Geotherm*  
887 *Res* 301:90–106

888 Torrente MM, Milia A (2013) Volcanism and faulting of the Campania margin (Eastern  
889 Tyrrhenian Sea, Italy): a three-dimensional visualization of a new volcanic field off Campi  
890 Flegrei. *Bull Volcanol* 75, DOI:10.1007/s00445-013-0719-0

891 Trincardi F, Field ME (1991) Geometry, lateral variation, and preservation of downlapping  
892 regressive shelf deposits; eastern Tyrrhenian Sea margin, Italy. *J Sedimentary Petrology*  
893 61:775–790

894 Vignaroli, G, Berardi G, Billi A, Kele S, Rossetti F, Soligo M, Bernasconi SM, (2016)  
895 Tectonics, hydrothermalism, and paleoclimate recorded by Quaternary travertines and their  
896 spatio-temporal distribution in the Albegna basin, central Italy: insights on Tyrrhenian  
897 margin neotectonics, *Lithosphere* L507.1, DOI:10.1130/L507.1

- 898 Weiss BJ, H\_bscher C, Wolf D, L\_dmann T (2015) Submarine explosive volcanism in the  
899 southeastern Terceira Rift/S\_o Miguel region (Azores). *J Volcanol Geotherm Res* 303:79–  
900 91
- 901 Yilmaz D (2001) *Seismic data analysis: processing, inversion and interpretation of seismic*  
902 *data. society of exploration geophysicists, series: Investigation in Geophysics 10, Tulsa,*  
903 *OK, ISBN 10: 1560800984.*
- 904 Yoon SH, Sohn YK, Chough SK (2014) Tectonic, sedimentary, and volcanic evolution of a  
905 back-arc basin in the East Sea (Sea of Japan). *Mar Geol* 352:70–88
- 906 Zitellini N, Marani M, Borsetti AM (1984) Post-orogenic tectonic evolution of Palmarola and  
907 Ventotene basins (Pontine archipelago). *Mem Soc Geol It* 27:121–131
- 908 Zitellini N, Trincardi F, Marani M, Fabbri A (1986) Neogene tectonics of the Northern  
909 Tyrrhenian Sea. *Gior Geol* 48:25–40

910

## 911 **Figure Captions**

912 Figure 1: Bathymetric map of the Latium and Campanian margin showing the volcanic Pontine  
913 archipelago and Ventotene basin (from **European Marine Observation and Data Network,**  
914 **EMODnet <http://www.emodnet.eu>**). The red box is the study area shown in Fig. 2, Yellow box  
915 locates the magnetic map in Fig. 6. **The black lines indicate the locations of multichannel and**  
916 **single channel seismic profiles: TIR10-17 in Fig. 3, V212 in Fig. 4c, profiles 165 and 107 in Figs**  
917 **5a and 5c, TIR10-13 in Fig. 9. The green line is the chirp profile 66 reported in figure 4a. The**  
918 **blue line is the TIR10-13 segment shown in Fig. 9. Red symbols represent volcanic edifices or**  
919 **complexes.**

920  
921  
922  
923 Figure 2: Morphological (a) and multibeam reflectivity (b) maps of the Ventotene Volcanic  
924 Ridge (VR) with location of seismic profiles and ROV dives. High backscattering strength  
925 interpreted as originating from localized rock outcrops (extreme backscattering) and widespread  
926 coarse sediment (remaining high backscattering) on the summits of edifices A, B, C1, and C2.  
927 The white arrows RD 1,2,3,4 indicate the ROV dives. **The white lines indicate the locations of**  
928 **multichannel and single channel seismic profiles: TIR10-17 in Fig. 3, V212 in Fig. 4c, profiles**  
929 **165 and 107 in Figs 5a and 5c. The green line is the chirp profile 66 reported in figure 4a.**  
930 Coordinates are distances (m) in Universal Transverse Mercator, Zone 33 (UTM33).

931  
932  
933  
934 Figure 3: Post-stack time-migrated **multichannel** section TIR10-17 (TWT s) (upper panel) and  
935 line drawing interpretation (lower panel) **Profile location in Fig. 1.** The black line is the main  
936 basal unconformity marking the basin substratum The overlying reflections (e.g., green, orange  
937 and yellow) constitute a Plio-Pleistocene syn and post extensional tectonics siliciclastic  
938 sequence. Red segments is the extensional and/or transtensional fault systems, Purple reflection  
939 shows the seismic interpretation of the A volcanic edifice. A and B denote location of the two  
940 volcanic edifices A and B. See text for the details of the interpretation

941  
942  
943

944 Figure 4: a) Chirp profile 66 across edifice A and SW-NE escarpment (profile location Figs. 1  
945 and 2); b) enlargement of profile 66 showing the summit of edifice A; c) chirp profile V212  
946 across edifice A (profile location Figs. 1 and 2); d) enlargement of profile TIR10-17 across  
947 edifice A (profile location Fig. 1); e) interpretation of profile TIR10-17 showing the acoustic  
948 basement and wedge-shaped prograding deposits W1 and W2.

949

950

951

952 Figure 5: a) Chirp profile 165 across Edifice B and SW-NE escarpment (profile location Figs. 1  
953 and 2); b) enlargement of profile 165 showing the summit of edifice B; c) chirp profile 107  
954 showing the SW-NE escarpment (profile location Figs. 1 and 2).

955

956

957

958 Figure 6: a) Magnetic anomaly map with the magnetic lines acquired during the three cruises  
959 TIR-10 (dash line), GEOCAL 2014 (ecks line), BOLLE 2014 (solid line). b) The Reduce To  
960 Pole (RTP) magnetic anomaly map. The bold black line (1-2) locates the profile shown in the  
961 upper right inset, where the RTP (black line) maximum value corresponds with the highest  
962 bathymetric gradient (red line) across the escarpment of C1. Black thin contour lines are  
963 bathymetry contours every 25 m. Black and blue dashed lines are foot and summit respectively  
964 of the edifices A, B, C1, and C2, as shown in Fig. 2. Coordinates are distances (m) in Universal  
965 Transverse Mercator, Zone 33 (UTM33).

966

967

968

969 Figure 7: ROV images from dives RD1, RD2 and RD3, RD4 along the upper and lower portion  
970 of the escarpment C1, respectively at depth of 294 ,278, 380 and 417 m (location in Fig. 2),  
971 which show the morphology of rocky seabed, probably of volcanic rocks.

972

973

974

975 Figure 8: The Reduced To Pole magnetic anomaly of the aeromagnetic map of Italy (Caratori  
976 Tontini et al, 2004). Grey lines locate the magnetic survey lines of Fig. 6.

977

978

979

980 Figure 9: Segment AB of the TIR10-13 **multichannel** seismic line and location map (**profile**  
981 **location Fig. 1**). a) Seismic line along to the northern base of Ventotene Island showing the lack  
982 of internal reflections within the volcanic rocks, whereas some superficial stratified layers  
983 correspond to the hemipelagic deposits. b) Shaded relief map of Ventotene volcanic complex,  
984 isobaths each 100 m. The red dashed line indicates the base of Ventotene edifice, the yellow  
985 represents the outer edge of insular shelf and blue line indicates the caldera rim. c), d)  
986 Enlargement of volcanic structures.

987

988

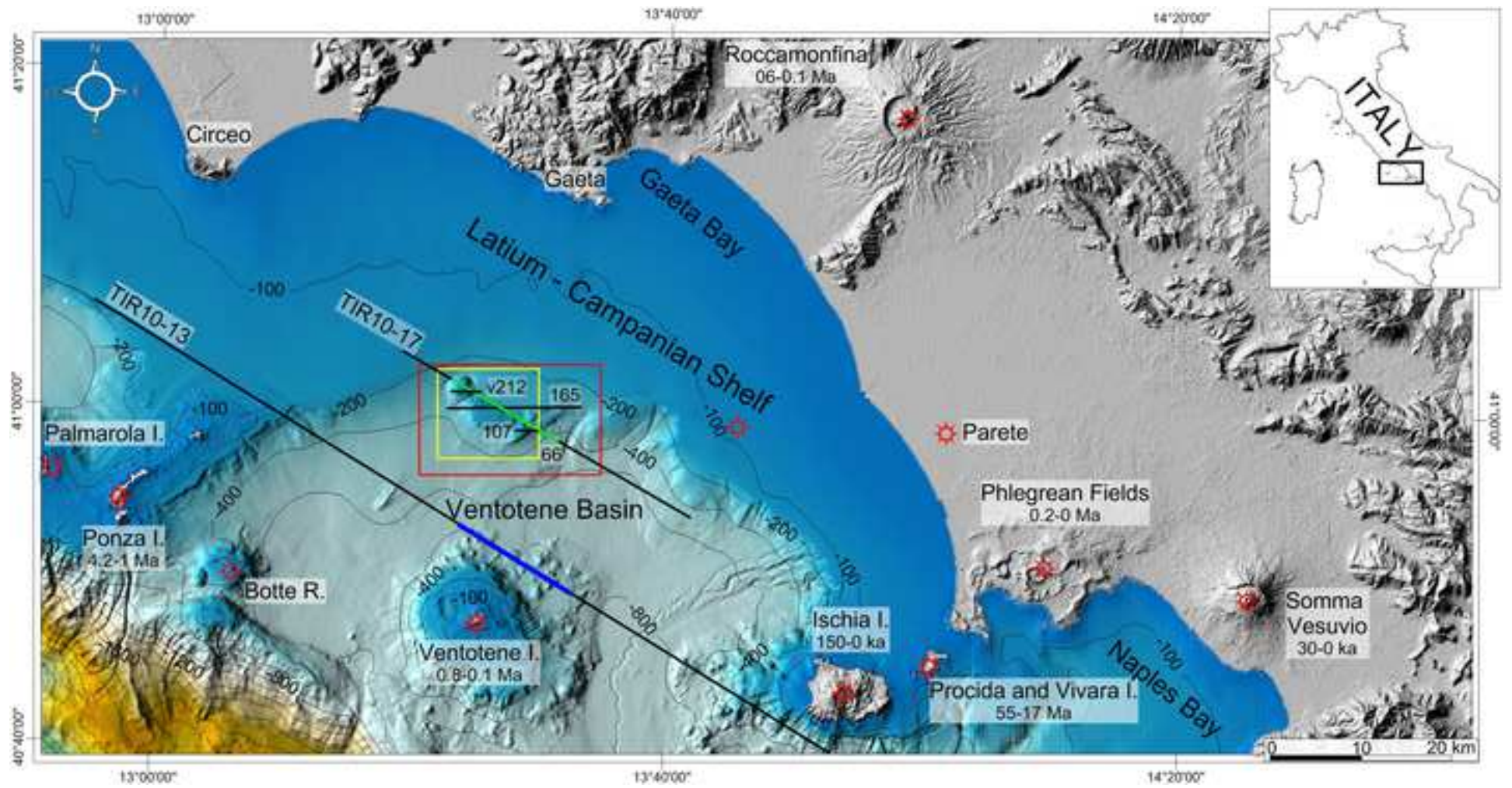
989

990 Figure 10: a) Selected bathymetric sections across edifices A and B (see Fig. 10b for location);  
991 b) slope maps of edifices A and B. Both these edifices have a flat summit with a smooth  
992 morphology and their flanks have slope angles  $< 20-25^\circ$ . **Coordinates are distances (m) in**  
993 **Universal Transverse Mercator, Zone 33 (UTM33)**. See text for discussion.

994  
995  
996  
997 Figure 11: Two-way time (TWT, ms) structural map of the main basal unconformity (black line  
998 in Fig. 3, top Messinian?) with bathymetric shaded relief. The structural map has been obtained  
999 combining information from seismic profiles of the TIR-10 survey (blue lines), of the CROP  
1000 database ([www.crop.cnr.it](http://www.crop.cnr.it)) (pink lines), and of the VIDEPI project  
1001 ([www.unmig.sviluppoeconomico.gov.it/videpi/en/sismica/sismica.asp](http://www.unmig.sviluppoeconomico.gov.it/videpi/en/sismica/sismica.asp)) (red lines). Black lines  
1002 are the interpreted normal faults. VR – Ventotene Volcanic Ridge. Red symbols represent  
1003 volcanic edifices or complexes. **Coordinates are distances (m) in Universal Transverse Mercator,  
1004 Zone 33 (UTM33).** Figure modified after Conti (2014).  
1005

Figure 1

[Click here to download Figure cuffaro16\\_figure1\\_rev\\_R1.jpg](#)



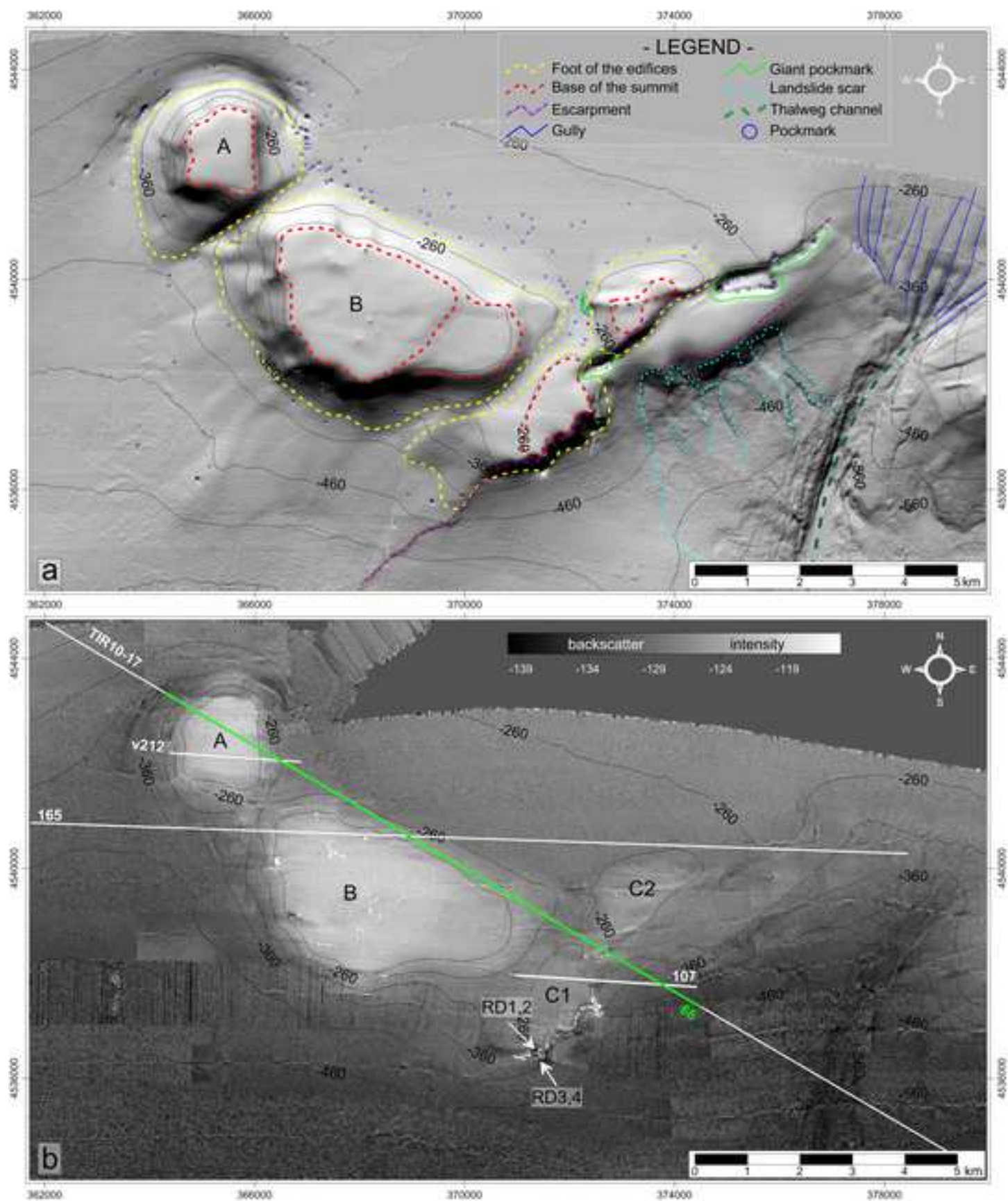
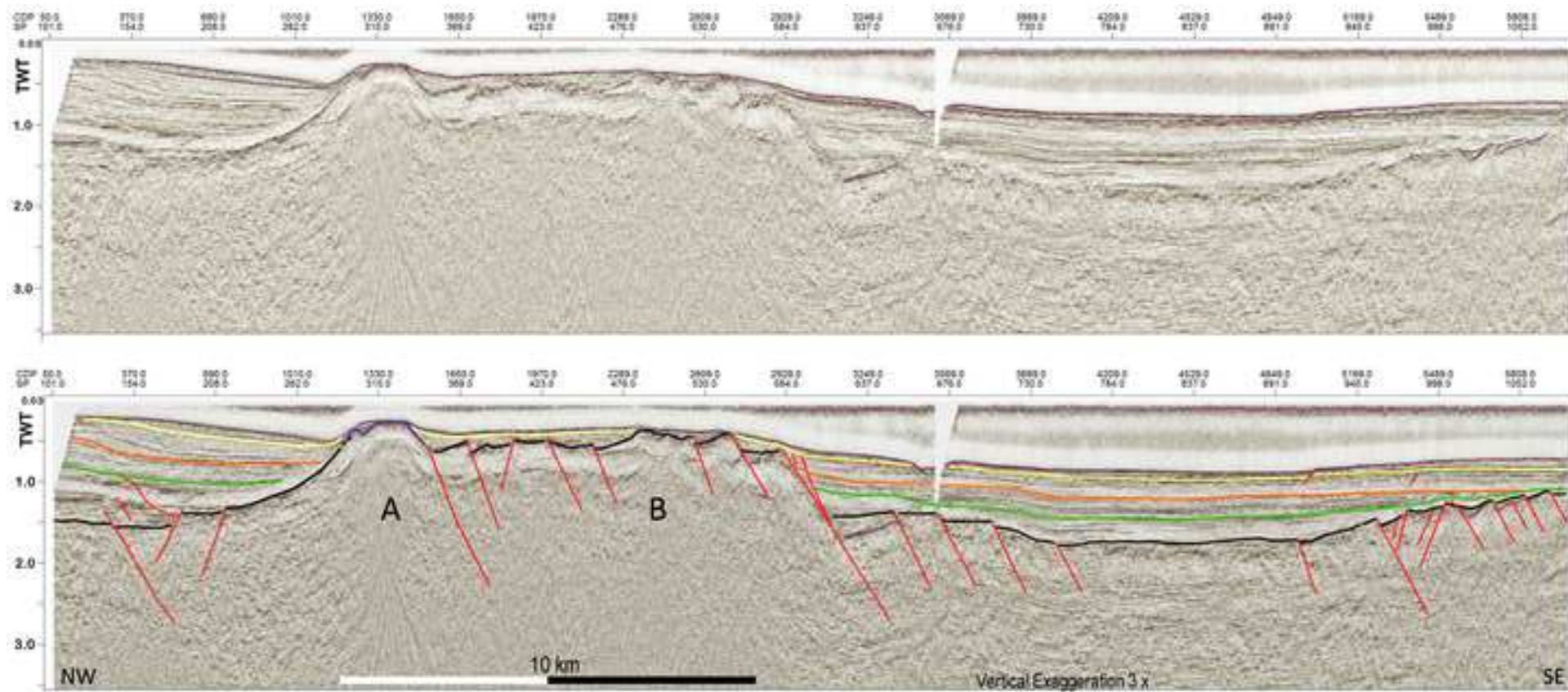
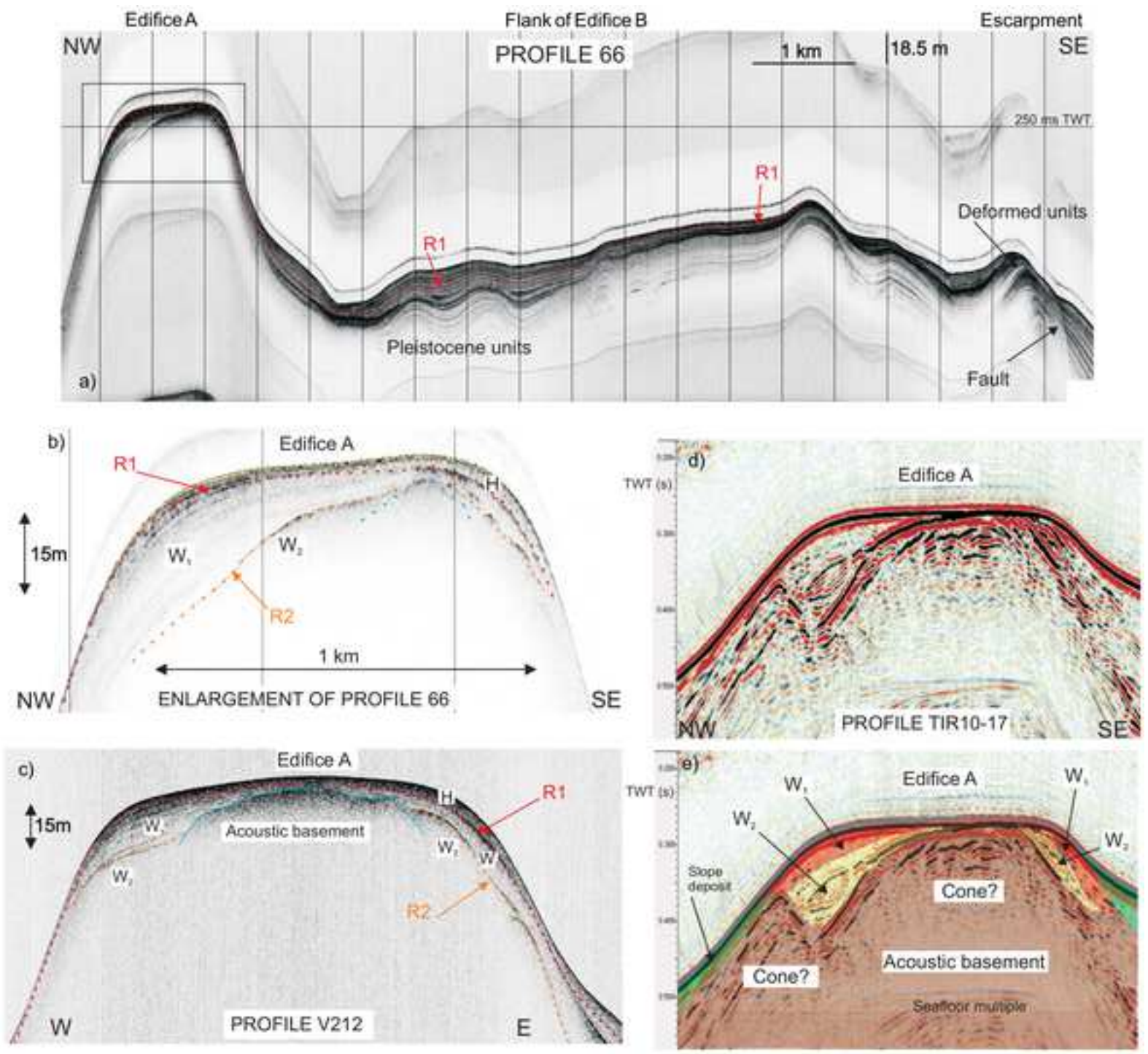
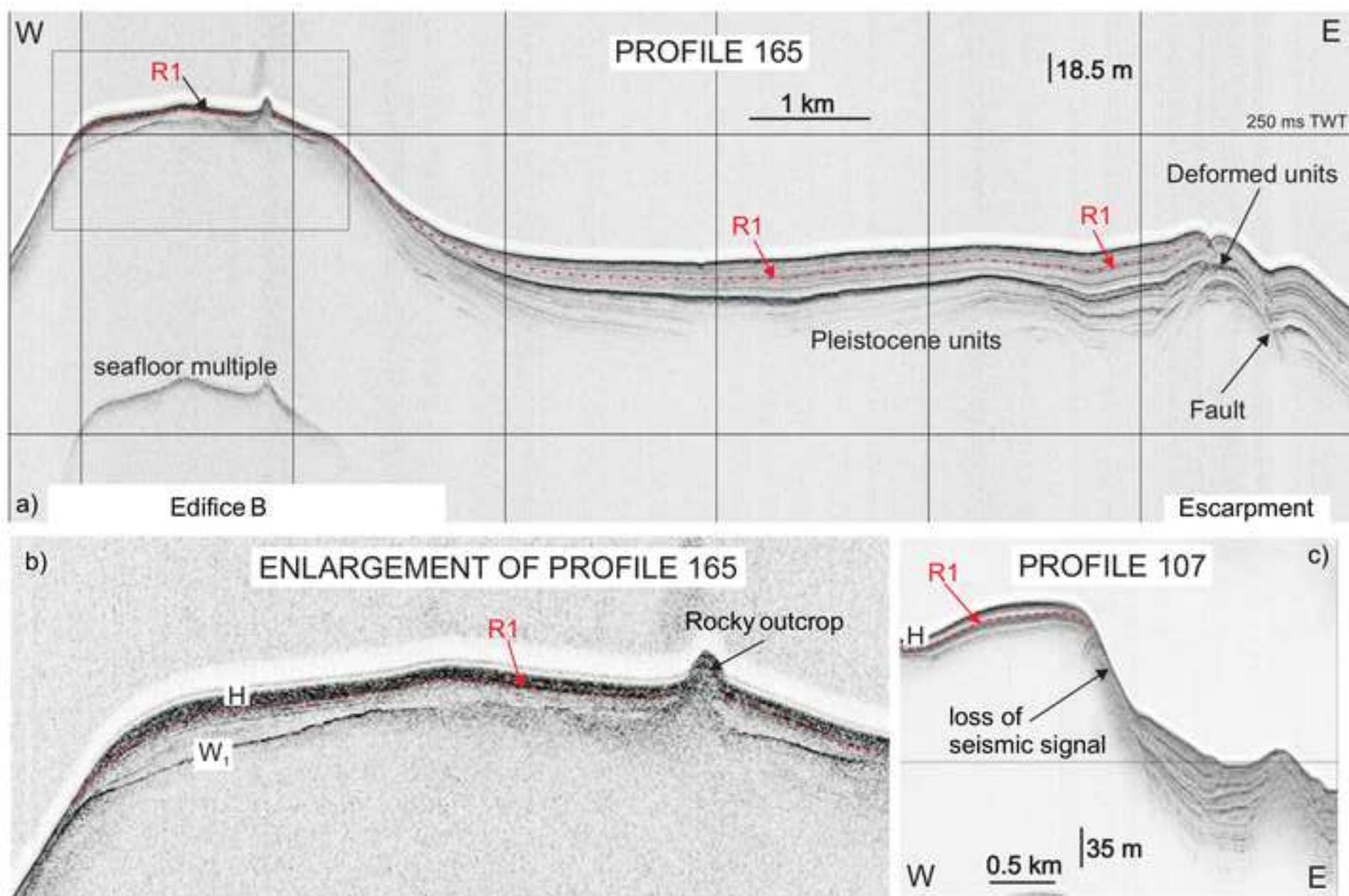


Figure 3







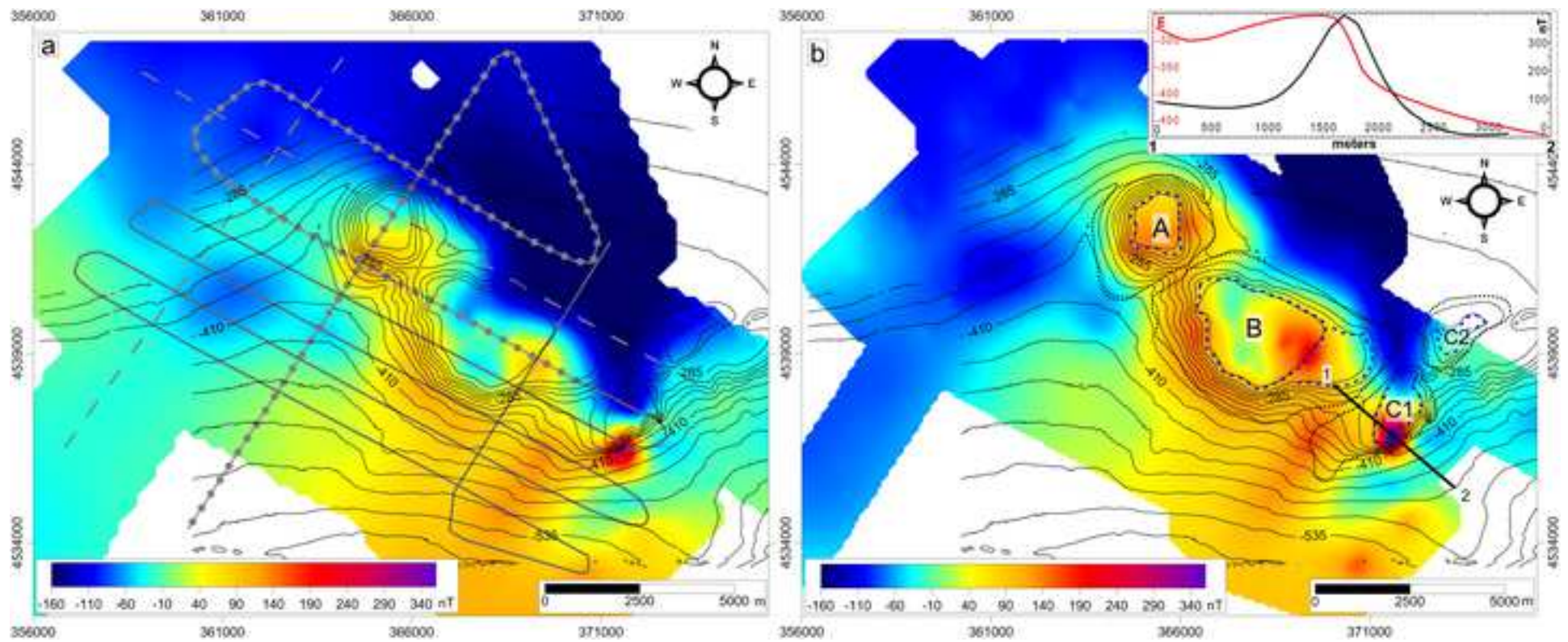
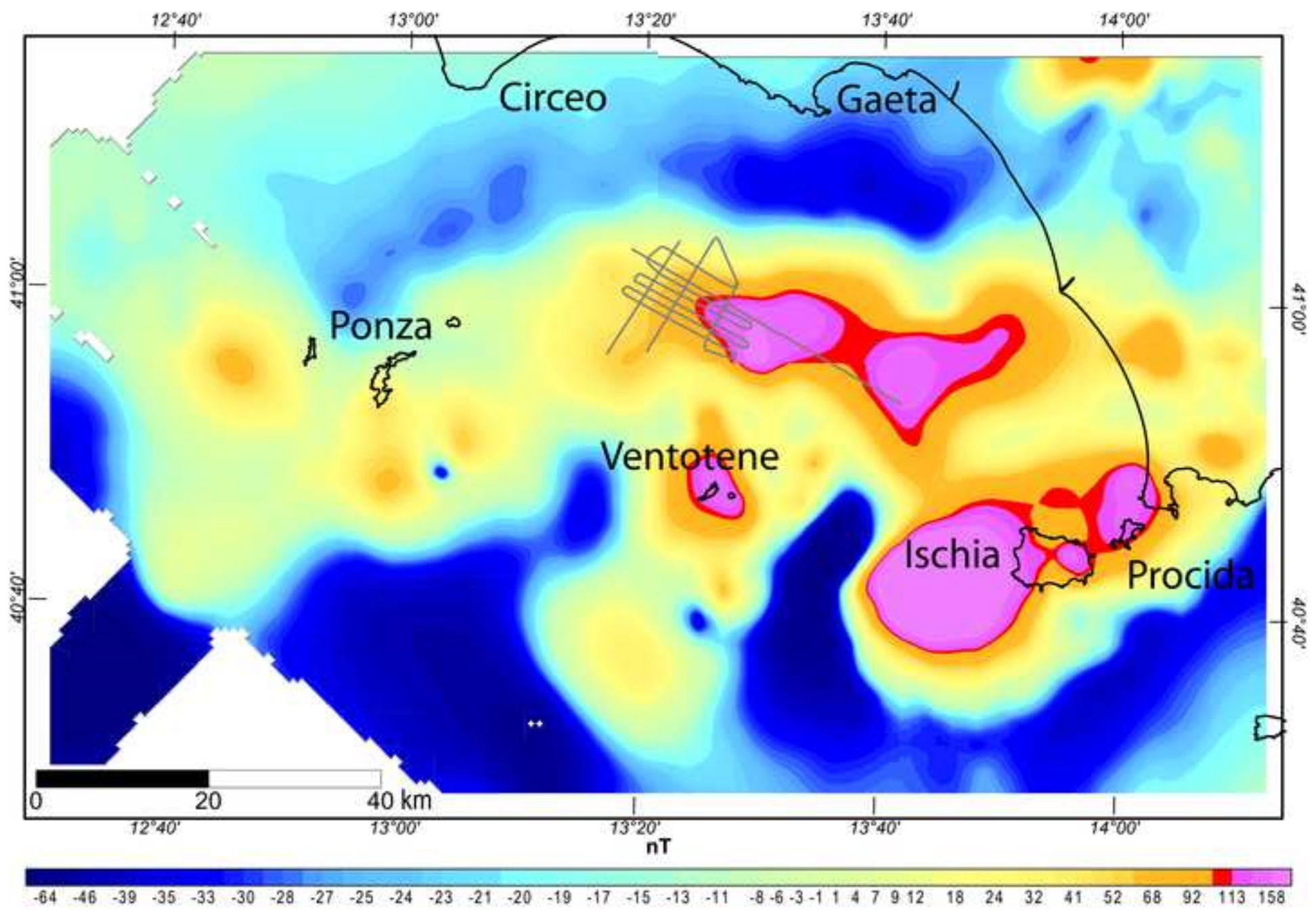
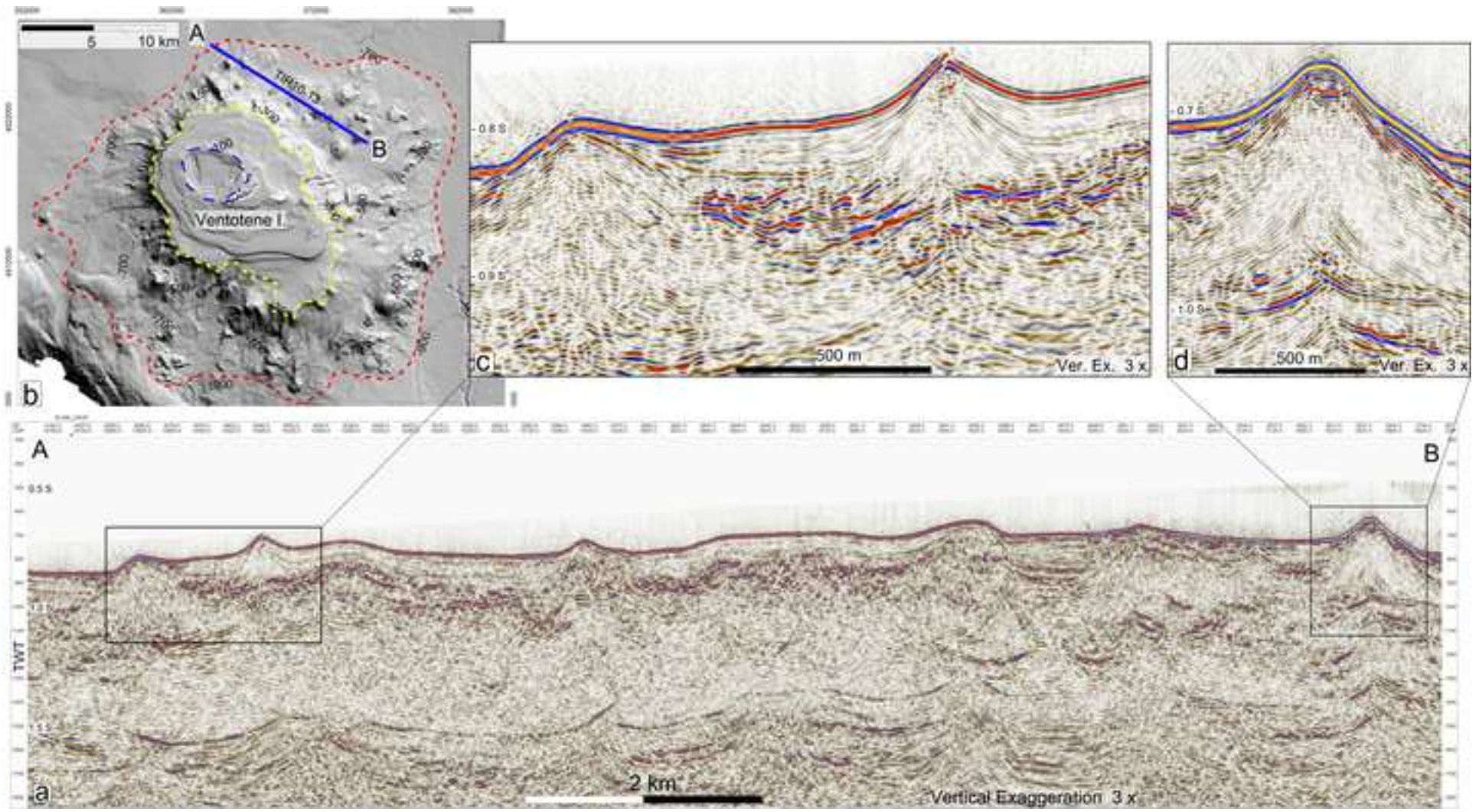




Figure 8





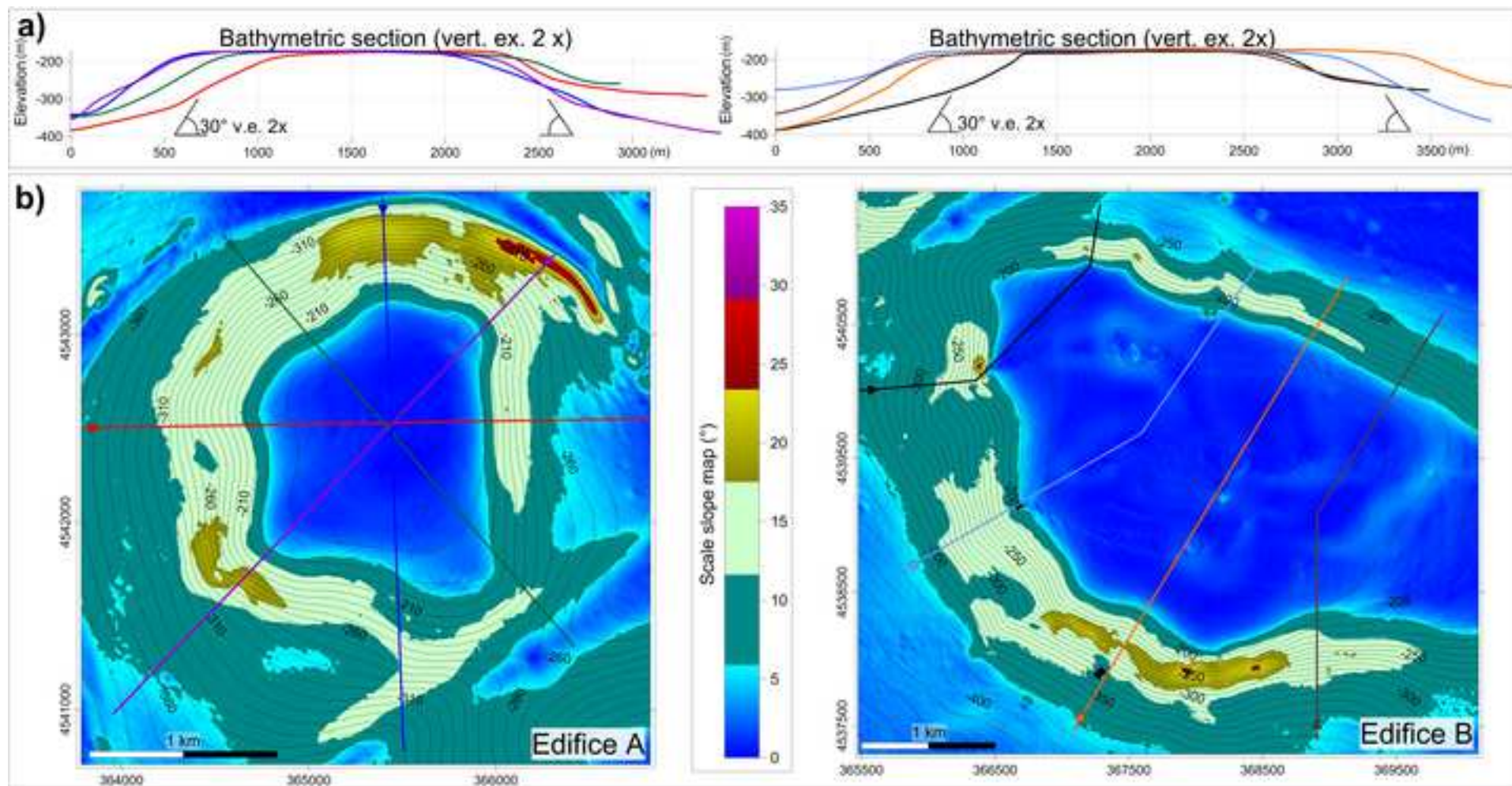


Figure 11

